AIAA Undergraduate Individual Aircraft Design

David Moeller Sztajnbok

May 2024

StratoSOL

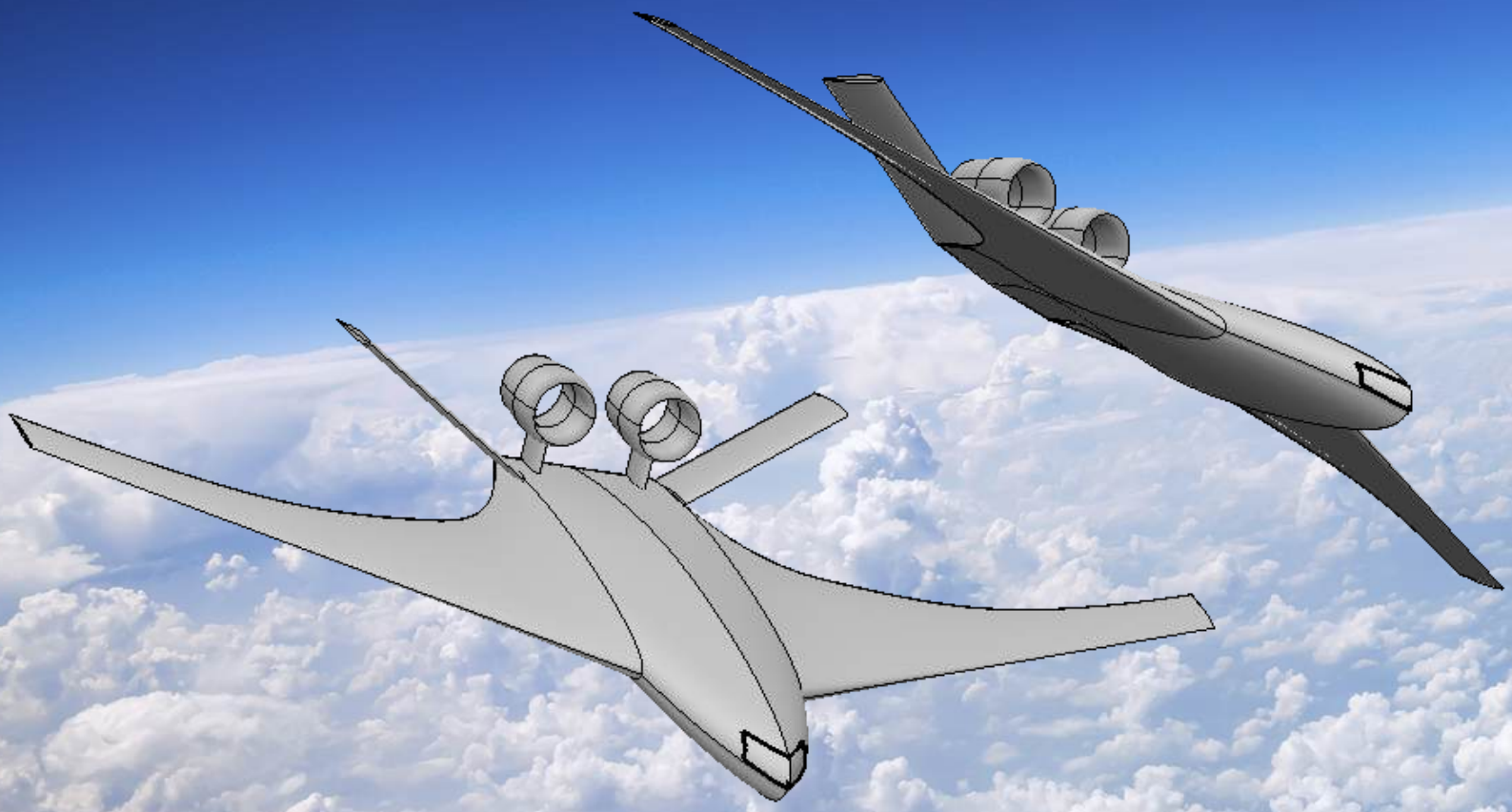

USC University of Southern California

David Moeller Sztajnbok

Name	AIAA Number	Signature
David Moeller Sztajnbok	**1255637**	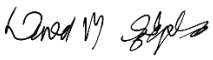

Faculty Advisor	AIAA Number	Signature
Dr. Geoffrey R. Spedding	**233796**	

Acknowledgements

A special thanks to:

Dr. Geoffrey Spedding for once again agreeing to advise me on this project so promptly and for putting up with my conflicting schedules, busy weekdays, digressions during meetings, and much more – and, of course, for the crucial help throughout the writing of this report!

And to:

Family and Friends who have supported me during this eventful year that marks the conclusion of half of my undergraduate degree.

Table of Contents

List of Figures

List of Tables

Chapter 1 – Introduction

1.1 Executive Summary

This report will show the sizing, design, and analysis of a novel aircraft – StratoSOL – capable of lofting 30,000 lb of aerosol up to 65,000 ft and operating 400 nmi missions at a significant aerodynamic advantage than previously proposed aircraft. The aircraft is to enter service by 2031.

This report will show that the design converged at a novel, hybrid wing body configuration powered by two high bypass-ratio turbofans mounted in the aft section of the wing-body. A V-Tail configuration gives the hybrid wing acceptable margins for center of gravity and stability & control considerations. Careful layout and weight & balance will show the stability of the configuration across flight all missions.

1.2 Solar Radiation Management

Over recent years, significant concern over the increase in the average temperature of the Earth due to human activity, industrial or otherwise, has given rise to research and investigation into ways to reduce the change of climate patterns observed – climate change. The origin of climate change stems from perturbations to the Earth's Energy balance, well described by the Trenberth Diagram (Figure 1-1)[1].

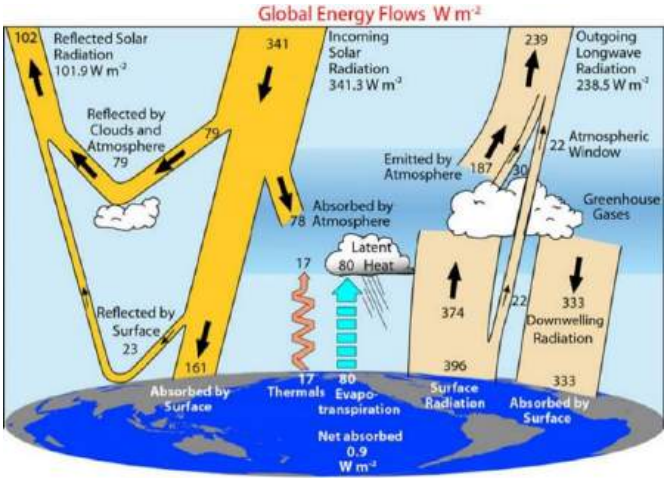

Figure 1-1: The Trenberth Diagram

Part of the solar radiation is reflected by the atmosphere, and its amount is determined by the Earth's reflectivity (or albedo.) However, part of the radiation is absorbed by the atmosphere, and high concentrations of what are called greenhouse gases – which includes carbon dioxide emitted by several combustion processes – increase the absorption of this radiation, which is radiated back into the Earth, increasing the average temperature, melting the polar caps, and several other consequences known to us as climate change. Several policies and recent research have indicated and suggested methods to reduce the "greenhouse effect," that is, reducing the absorption effectiveness of the Earth's atmosphere.

The Intergovernmental Panel on Climate Change (IPCC) published a special report in 2018 titled "Global Warming of 1.5ºC" where it outlined the consequences of reaching a mean increase of 1.5º in temperature in post-industrial times for the planet, as well as a summary of policies to be adopted by governments across the world to keep the average temperature rise below the stipulated limit[2]. Most of these policies rely on carbon capture and sequestration methods to reduce the parts-per-million (ppm) of greenhouse gases in the atmosphere, as well as policies for the reduction of greenhouse gases emissions in the first place. However, for the first time, the panel also considered a novel approach to combating climate change: solar radiation management.

Carbon capture and sequestration methods reduce the absorption of the Earth's atmosphere. However, Solar Radiation Management (SRM) and similar methods aim to increase the Earth's albedo, that is, the reflection of the incoming solar radiation. One way to achieve this is the concept of Stratospheric Aerosol Injection (SAI,) wherein thin reflective particles are released in the upper atmosphere and dispersed, where they reflect part of the incoming solar radiation, increasing the Earth's albedo. Research is still being conducted on the effects of SAI, and interesting comparisons have been made using data from space shuttle rocket launches[3] and volcanic eruptions[4]. However, it has been estimated that ~1-5M metric tons would be required per year to sustain an increase in 1-4 watts/m^2 in solar radiation reflection.

Recent studies have also concluded that the most economically feasible approach to a large-scale geoengineering approach to climate change through SAI is the design and development of a brand-new stratospheric payload delivery platform[5]. This platform would incorporate existing engine technology and perform a SAI mission at ~65,000 ft in the upper atmosphere. There is a very well established market for military and commercial high-payload platforms for operation in the lower atmosphere, but no existing one for operation in the upper atmosphere. This report will show the conceptual design of such platform - StratoSOL.

1.3 Review of Requirements

The RFP[6] lays out general requirements for all flying missions as well as mission-specific requirements. The aircraft will be designed for two flying missions.

The general requirements are as follows: the aircraft must be able to takeoff and land from concrete. It must cruise at a Mach Number at or above 5. It must fly in VFR and IFR, as well as being capable of flight into known icing conditions (FIKI.) These latter two points imply stricter certification considerations and will be discussed later.

The RFP also lays out the following mission-specific requirements:

Table 1-1: Summary of Mission-Specific Design Requirements

Requirement	Payload Dispensing Mission	Ferry Mission
Crew	4 flight crew	4 flight crew
Payload	30,000 lb	0 lb
Range	400 nm	3000 nm
Cruise Altitude	65,000 ft	65,000 ft
Take-off and Landing	≤ 8,000' over 50' obstacle at: • ISA and ISA+61ºF • Sea-level and 2,500'	≤ 8,000' over 50' obstacle at: • ISA and ISA+61ºF • Sea-level and 2,500'
Additional / Miscellaneous	Time to climb ≤ 1 hour Payload contained in appropriate tank	-
Flying Qualities	CFR Part 23	CFR Part 23

Lastly, it is worth noting that the aircraft's expected entry into service (EIS) is 2031 and should therefore incorporate existing technology at the time and/or reasonable assumptions about said technology. Feasible economic analysis[5, 7] utilize existing technologies to reduce cost, and this philosophy will be continued here. This is especially true when it comes to the powerplant – development of a new engine can be as expensive as the rest of the design effort. An engine selection rather than a design will therefore be made.

The requirements above will be revisited when the design is completed.

1.4 Analysis of Competition

Analysis was conducted on aircraft of similar design missions than StratoSOL. As mentioned before, there are several aircraft designed for cargo missions in the transonic regime in the lower atmosphere. However, there are no well-established platforms for cargo at the upper atmosphere. An aircraft as such would be designed closer to high-altitude reconnaissance aircraft.

Three comparable aircraft were analyzed: Martin's RB-57F, Lockheed's U-2S, and Ryan's AQM-91. An overview of their design is explored below.

The Martin RB-57F was designed from the B-57 Canberra with several modifications to allow flight in the upper atmosphere for the purposes of surveillance and reconnaissance. The aircraft features a strikingly large-area wing and a large wingspan of around 120 feet. It also featured an interesting design choice when it comes to the powerplant: the aircraft was powered by two P&W TF33 turbofan engines buried in the wing, but also included two additional J60 turbojets that were started at altitude to increase the effective service ceiling of the aircraft, allowing it to climb to the reconnaissance altitudes it required. The aircraft is capable of carrying some 9,700 lb of payload. This stems from its large wing area and cruise speed at around Mach 0.78, allowing it to generate a lot of lift despite the high altitudes of operation. The aircraft is also reported to have a range close to 3000 mi and an endurance of over 6 hours[8].

Figure 1-2: Martin RB-57F

The Lockheed Martin U-2S is the newest variant of the U-2 "Dragon Lady" designed in the 1950s. The U-2 served as the United States' primary military surveillance aircraft, and was present in several geopolitical crises during the cold war and in the middle east.

Its design is very resemblant of the Martin RB-57F: it features a large wingspan, tapered planform, typical of aircraft that fly at high altitudes. It has a conventional tail. It is powered by a single General Electric F118-101 engine, with a pair of inlets lofted smoothly immediately behind the cockpit. The Dragon Lady has half the wing area of the Martin RB-57F but can carry much less payload, some estimated 3,750 lb. It cruises at around Mach 0.72 at altitudes above 65,000 ft. The aircraft is estimated to have a range of over 6000 nmi. This is attributed to its glider-like design, allowing it to reach lift-to-drag ratios of 23:1. An interesting note about the aircraft that is also typical of flight at such high altitudes is the thin margin between the structural limits of the airframe at the never exceed speed and the aerodynamic stall speed at high altitudes. This narrow region in the flight envelope is called the "coffin corner."


Figure 1-3: Lockheed U-2S

Lastly, the Ryan AQM-91 “Firefly” was an unmanned aerial vehicle (UAV) designed for military reconnaissance during the Vietnam war. The aircraft is at a different weight class than the two mentioned above but features design choices relevant to the problem at hand. The aircraft has much more wing sweep than either Lockheed’s U-2S or Martin’s RB-57F: some 28º of wing sweep. This helps to delay the formation of shock waves due to local supersonic speeds attained at the wind. The aircraft is powered by a single General Electric YJ97-GE-3 with an inlet smoothly lofted above the fuselage. It is reported that the top-mounted engine effectively reduces the aircraft’s radar cross section for stealth purposes. The aircraft features an H-Tail, possibly for operation from aircraft carriers. The UAV has a reported range of around 2000 nmi and a service ceiling well above 65,000 ft.

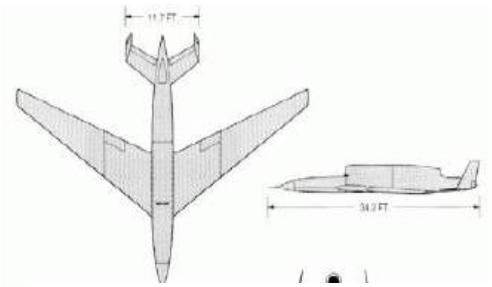

Figure 1-4: Ryan AQM-91 "Firefly"

Below are tables that summarize the performance and geometric parameters found for the aircraft detailed above. They were taken from miscellaneous sources. A comparison of these values is essential as it can give insight into the design space these aircraft lie in and guide the selection of design points such as wing loading, thrust-to-weight ratio, aerodynamic features, and many others.

Table 1-2: Performance Summary of Competitive Aircraft

Parameter	Martin RB-57F	Lockheed U-2S	Ryan AQM-91
TOGW [lb]	61,500	41,000	5,245
Max Fuel Weight [lb]	-	19,700	-
Empty Weight [lb]	36,900	16,000	3,800
W/S [lb/ft^2]	25	32	20
T/W [-]	0.67	0.57	1.05
Cruise Mach [-]	0.78	0.72	0.85
Take-Off Field Length [ft]	2,600	-	-
Range Max Freight [nm]	2,500	6,090	1,700
Service Ceiling [ft]	> 65,000	> 70,000	> 78,000

Table 1-3: Geometry Summary of Competitive Aircraft

Parameter	Martin RB-57F	Lockheed U-2S	Ryan AQM-91
Wing Area [ft^2]	2,000	1,000	250
Wingspan [ft]	123	103	47.7
Wing Aspect Ratio [-]	7.5	11	9.1
Wing Sweep Angle [deg]	6	4	28
Overall Length [ft]	68.3	63.0	34.2

1.5 Summary and Design

Flight at 65,000ft is a tremendous engineering challenge. To guide the following design, it is important to identify key similarities between the aircraft mentioned above.

Firstly, the planform design is crucial. A tradeoff between available wing area and cruise speed exists. Higher cruise speeds require less wing area for flight at the same air density. There is therefore a benefit of flying faster (higher wing loading) since it allows a decreased planform. The thrust required increases, but the parasite drag from the wing also decreases. This must be carefully balanced with compressible effects. Capturing all of these effects is challenging, but the following chapter will show parametric baseline trade studies that explore the constraints implied by these factors.

The engine selection is also crucial: all designs feature very high thrust-to-weight ratios. StratoSOL is expected to have even higher thrust-to-weight due to its heavier payload fraction than the aircraft above. Regardless, just as important as a powerful enough engine is a sleek enough aerodynamic design: the U2's glider like design yields an impressive lift-to-drag ratio, relaxing the thrust concerns of stratospheric flight with reduced drag. Other aerodynamic design aspects – wing sweep, airfoil selection for low thickness-to-chord ratio, etc. – are also crucial.

All of these ideas are considered throughout the design that will follow. First, an exploration of the design space is needed so that these parameters can be traded. This is conducted in the following chapter.

Chapter 2 – Constraint Analysis

2.1 Introduction

To evaluate the design space of StratoSOL, the performance constraints as published in the RFP were evaluated using the method of constraint analysis. The primary goal of this method is to determine two key performance parameters of the aircraft: the thrust-to-weight ratio T/W and the wing-loading W/S. This can be done by deriving expressions that involve the performance metric in question as well as these two parameters. A diagram can then be created with lines of T/W and W/S that satisfy the performance constraint. The plots below were generated using a Python-based suite of aircraft design and sizing codes written by this author, *DSAeroTools*. A lot of the analysis that follows was prepared using this code.

These expressions were taken from Gudmundsson[9]. Note that a few assumptions must be made. Namely, a rough guess of the minimum drag coefficient as well as drag and lift during take-off must be made. Also, for the climb-related constraints, an estimate of the best rate of climb airspeed, V_Y, must be made. Gudmundsson suggests a take-off drag coefficient and lift coefficient of 0.035 and 0.8, respectively, for turboprop-driven business jets. He also suggests a minimum drag coefficient between 0.02 and 0.025. A conservative 0.03 is used for the analysis below. Gudmundsson also presents values of V_Y for two different business jets. They are reproduced in the table below, and an intermediate value is chosen:

Table 2-1: Sample Aircraft V_Y

Aircraft	Gross Weight [lb]	V_Y [KCAS]
Beechjet 850XP	18,000	138
	24,000	161
	28,000	170
Gulfstream 450	40,000	128
	50,000	143
	60,000	157
	70,000	169
	80,000	181

2.2 Takeoff Constraint

Equation (1) constrains T/W and W/S for a given ground roll:

$$\frac{T}{W} = \frac{1.21}{(g\rho C_{L_{max}})S_g}\left(\frac{W}{S}\right) + \frac{0.605}{C_{L_{max}}}(C_{D\,TO} - \mu C_{L\,TO}) + \mu \tag{1}$$

The ground roll must be shown to be under 8,000' at an altitude of 2,500'. To account for higher density altitudes, the ground roll value was multiplied by a factor of 0.9 in the constraint analysis.

2.3 Cruise Speed Constraint

The minimum cruising speed as per the RFT is Mach 0.5 at the cruising altitude of 65,000ft. The constraining expression, Equation (2), is shown below:

$$\frac{T}{W} = q_{cruise}C_{D_{min}}\left(\frac{1}{W/S}\right) + k\left(\frac{1}{q_{cruise}}\right)\left(\frac{W}{S}\right) \tag{2}$$

However, at the altitudes of stratospheric flight, the impact of reduced density must be considered. The density ratio at 65,000ft is around 0.08, meaning that at first order an engine operating at that altitude will produce only 8% of the installed thrust at sea-level. This increases the required thrust by an order of magnitude. To account for this, Equation (2) is modified as shown below:

$$\frac{T}{W} = \left[q_{cruise}C_{D_{min}}\left(\frac{1}{W/S}\right) + k\left(\frac{1}{q_{cruise}}\right)\left(\frac{W}{S}\right)\right]\frac{1}{\sigma} \tag{3}$$

Which places a significant constraint on the required thrust to weight ratio to maintain steady-level flight at 65,000ft. Below is the required thrust-to-weight ratio versus wing-loading at various cruising Mach numbers at altitude:

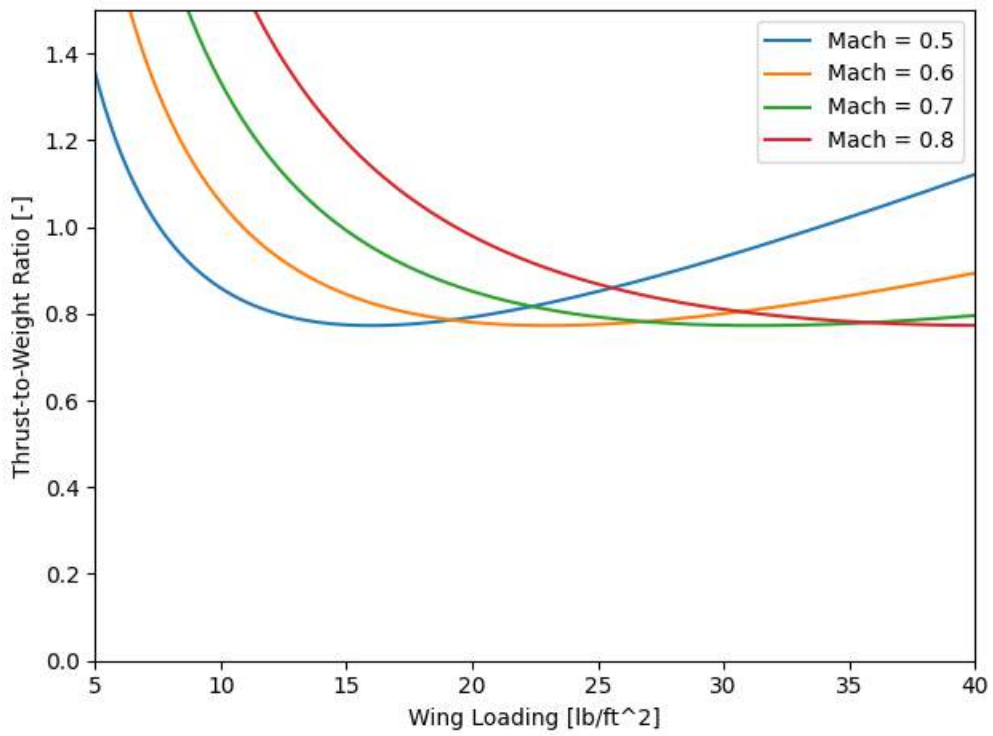

Figure 2-1: Cruise Mach Constraint

From the study above, a cruise Mach of 0.7 is selected. The curve offers a minimum thrust-to-weight ratio at a higher wing-loading, allowing for a reduced wing area while remaining clear of drag divergence at transonic speeds.

2.4 Service Ceiling Constraint

A service ceiling is not specified in the RFP. To design with tight margins, a service ceiling equal to the cruise altitude of 65,000ft will be assumed, such that the aircraft can climb to the cruise altitude and have some remaining excess thrust to climb at 100 fpm. A few best ROC speeds, V_Y, were assumed and varied. The constraining expression, Equation (4), for the service ceiling is shown below:

$$\frac{T}{W} = \frac{1.667}{V_Y} + \frac{q_{V_Y}}{(W/S)} C_{D_{min}} + \frac{k}{q_{V_Y}} \left(\frac{W}{S}\right) \tag{4}$$

This, along with the cruising Mach number, are the primary performance constraints on the aircraft.

2.5 Rate of Climb Constraint

Lastly, a constraint on rate of climb (ROC) was also placed. The expression is shown in Equation (5):

$$\frac{T}{W} = \frac{V_V}{V_\infty} + \frac{q}{(W/S)} C_{D_{min}} + \frac{k}{q}\left(\frac{W}{S}\right) \tag{5}$$

The RFP calls for a time to climb to cruising altitude of under an hour. This yields an average ROC of roughly 1,100 fpm. However, altitude effects must be accounted for, such that the ROC at sea level is higher than the average. If the maximum ROC decreases roughly proportionally to the altitude, then the required sea level ROC for a service ceiling of 65,000ft can be approximated as 2100 fpm. This value is used for the analysis.

2.6 Selection of T/W and W/S

The constraints analyzed above can be put together to identify feasible regions of the design space. The selected design point will thus satisfy all performance requirements. The full constraint analysis diagram is shown below and includes all previously studied performance constraints, selecting the most conservative options (lowest $C_{L_{max}}$, highest RoC, etc.):

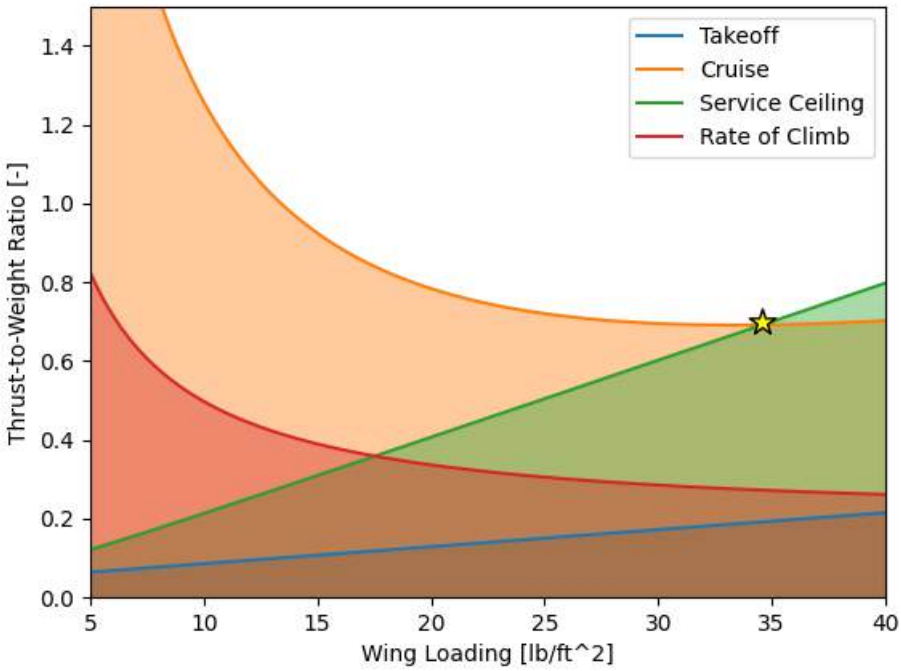

Figure 2-2: Final Constraint Diagram

The initial design point for StratoSOL is thus selected to be:

Table 2-2: Initial Design Point

Parameter	Initial Value
W/S	35 lb/ft^2
T/W	0.7

And is labelled in the constraint diagram. These values can be parametrically varied to evaluate sensitivity to wing-loading and thrust-to-weight ratio. This is done in the following chapter, along with other trade studies to optimize the design point.

Chapter 3 – Mission Analysis and Initial Sizing

3.1 Summary of Sizing Method

An initial value for the aircraft's takeoff gross weight W_0 was estimated using the method of mission analysis, explained at length in Gudmundsson[9] and Raymer[10]. An aircraft's take-off weight can be written as:

$$W_0 = \frac{W_c + W_p}{1 - \frac{W_e}{W_0} - \frac{W_f}{W_0}} \tag{6}$$

Known as the unity equation, where W_c and W_p are the crew and payload weights, specified in the RFP. The fraction $\frac{W_e}{W_0}$ is the empty weight fraction, which can be estimated by statistically fitting the empty weight versus the takeoff gross weight of aircraft of the same class in a power equation, such that:

$$\frac{W_e}{W_0} = AW_0^B$$

And the fuel fraction, $\frac{W_f}{W_0}$, can be estimated by analyzing the aircraft's design mission. A mission's *segment* is one "leg" of a mission, that is, the cruise, climb, descent, etc. Let W_i be the weight of the aircraft in segment i of a mission with N segments. We can find the total fuel expenditure by taking the product of all fuel fractions across the mission, that is:

$$\frac{W_f}{W_0} = 1 - \frac{W_1}{W_0}\frac{W_2}{W_1}\frac{W_3}{W_2}\frac{W_4}{W_3}\ldots = 1 - \prod_1^N \frac{W_i}{W_{i-1}}$$

Where the fuel fraction of each segment can be estimated using methods in the references cited above. Notice that solving for W_0 requires an iterative solution to the unity equation. The method can be further improved by guessing the increase in expected thrust-to-weight ratio in climb segments, $r_i = \frac{T_{max}}{W_0}\frac{W_0}{W_i}$ due to the fuel burn before that segment. Then, once a solution converges for W_0, these ratios can be re-computed with the actual weight at segment i, and the entire process repeated. This procedure is explained in detail in [9].

3.2 Mission Profile and Assumptions

The methods in [9] and [10] were incorporated into the sizing codes in DSAeroTools, written by this author. The mission profile for StratoSOL is shown below:

Table 3-1: StratoSOL Mission Profile Description

Mission Segment	Description	Performance Metrics
1 – 2	Taxi & Takeoff	-
2 – 3	Climb	SL to 65,000 ft
3 – 4	Cruise + Payload Drop	400 nmi M = 0.8 (Cruise Speed Traded)
4 – 5	Descent	65,000 ft to 5,000 ft
5 – 6	Loiter	30 min
6 – 7	Descent	5,000 ft to SL
7 – 8	Landing & Shutdown	-

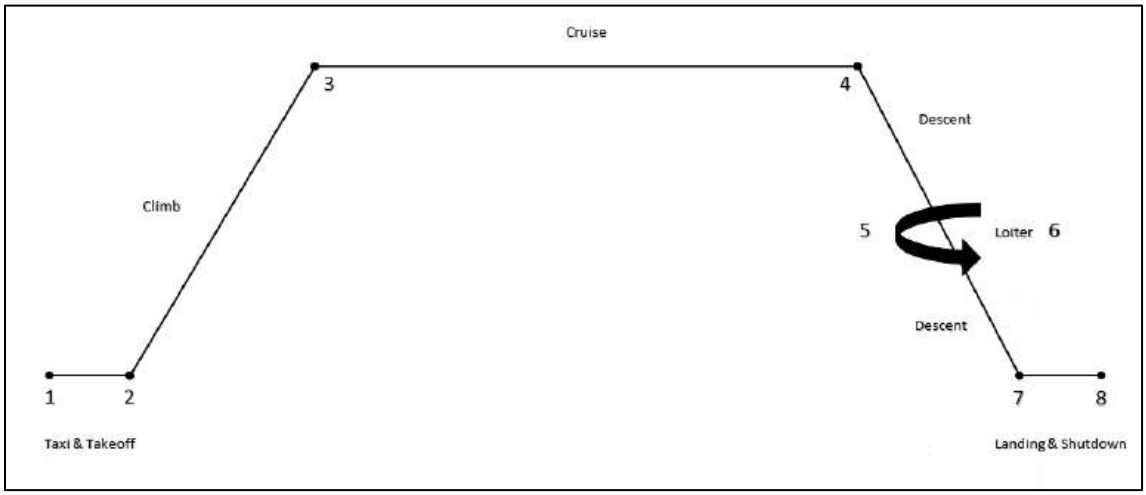

Figure 3-1: StratoSOL Mission Profile

A few assumptions must be stated. First, a specific fuel consumption of 0.5 1/hr was assumed, reasonable for high-bypass ratio turbofans and in agreement with suggestions in Raymer[10] and Gudmundsson[9]. Additionally,

Raymer[10] presents a method to estimate the maximum lift-to-drag ratio using a selected aspect ratio and a wetted area ratio, as shown in the Equation (7):

$$\left(\frac{L}{D}\right)_{max} = K_{LD}\sqrt{\frac{AR}{(S_{wet}/S_{ref})}} \tag{7}$$

The wetted area ratio can be "eyeballed" using a diagram provided in the textbook. The configuration downselect in the next chapter will show the selection of a Blended Wing Body configuration. One benefit of such configuration is clear here: its lower wetted area ratio (taken to be 2) allows for a more effective lifting body, yielding higher lift-to-drag ratio and improvements in performance. This comes with configuration and stability challenges.

The aspect ratio is selected, and an initial value of 10 is assumed based on similar aircraft (Table 1-3). A statistical fit method also in Raymer confirms the value. Finally, the empty weight fraction for the iterations is found with:

$$\frac{W_e}{W_0} = 0.93W_0^{-0.07}$$

And the constants are found by statistical regression of similar aircraft, found also in Raymer.

3.3 Mission Analysis

The mission profile was analyzed iteratively. An assumed weight of 240 lb per crew member is used, which includes flight gear. Below is the result of the iterations:

Table 3-2: Initial Weights

Parameter	Initial Value
W_0	171,440 lb
W_{empty}	68,581 lb
W_{fuel}	43,333 lb

Chapter 4 – Design Space Trade Studies

4.1 Introduction

Before settling on a design point, it is important to evaluate the sensitivity of changes in thrust-to-weight ratio and wing loading to key performance parameters. It is also possible to iterate through the mission analysis with varying parameters to study their effect on take-off gross weight. This study is conducted below.

4.2 Take-off Gross Weight Sensitivity

The mission profile analysis of chapter 3 was repeated iteratively with varying parameters to investigate the effect of cruise number and range on the target W_0. The studies are shown below:

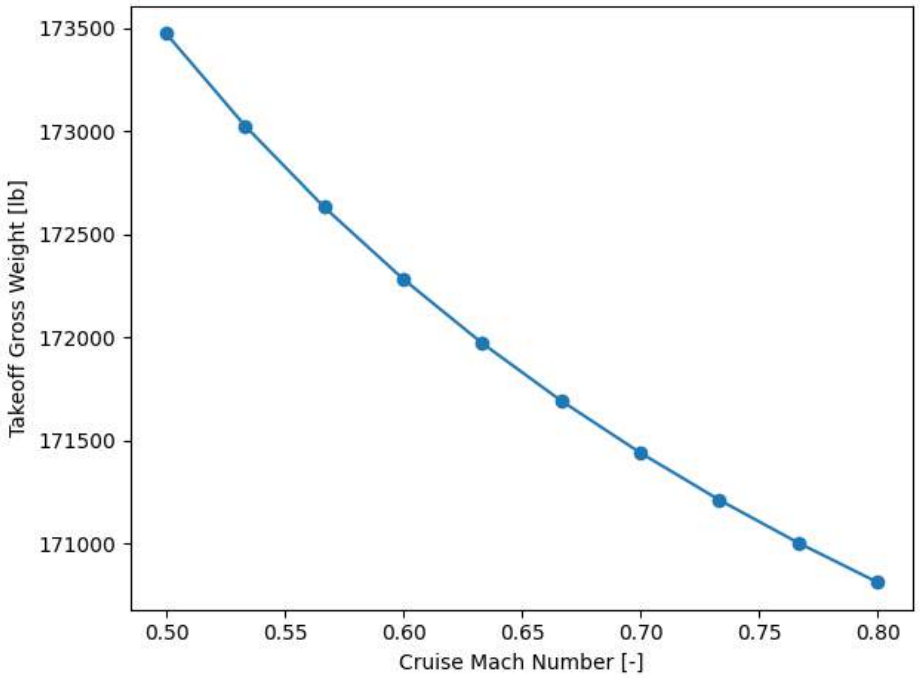

Figure 4-1: Cruise Mach Trade Study

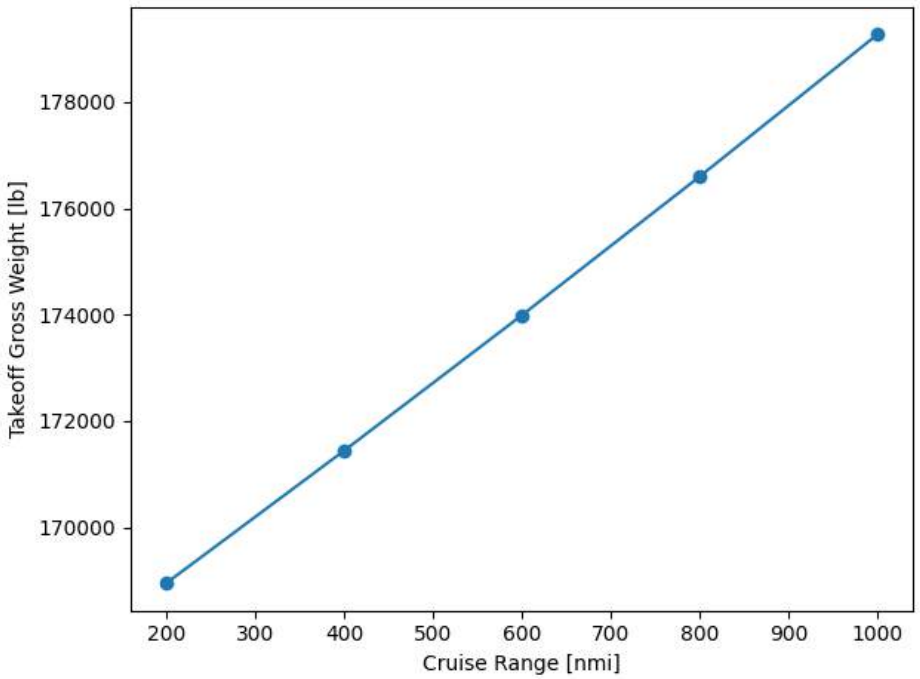

Figure 4-2: Range Trade Study

It is shown to first order that increasing the Mach during cruise decreases the takeoff gross weight. A higher cruising airspeed allows for the same lift to be attained by a relatively smaller wing, reducing structural weight. However, a powerplant that is able to sustain level flight at such Mach numbers must be selected. The following chapters will show such selection.

Secondly, for every nautical mile of additional range, some estimated ~10lb of takeoff gross weight are required. This is an important consideration for initial sizing, though the chosen design point reflects accurately the RFPs design mission and will thus be kept until further analysis.

4.3 Baseline Parametric Trade Study

A baseline parametric study of the design space was also conducted. Equations (1) through (5) can be solved for their respective performance metric, with which the selected T/W and W/S can be varied parametrically and a performance metric compared across the range.

The selected T/W and W/S were varied within 10% of the initial design point, and three key performance metrics were compared: takeoff distance, service ceiling, and sea-level rate-of-climb. They are shown below:

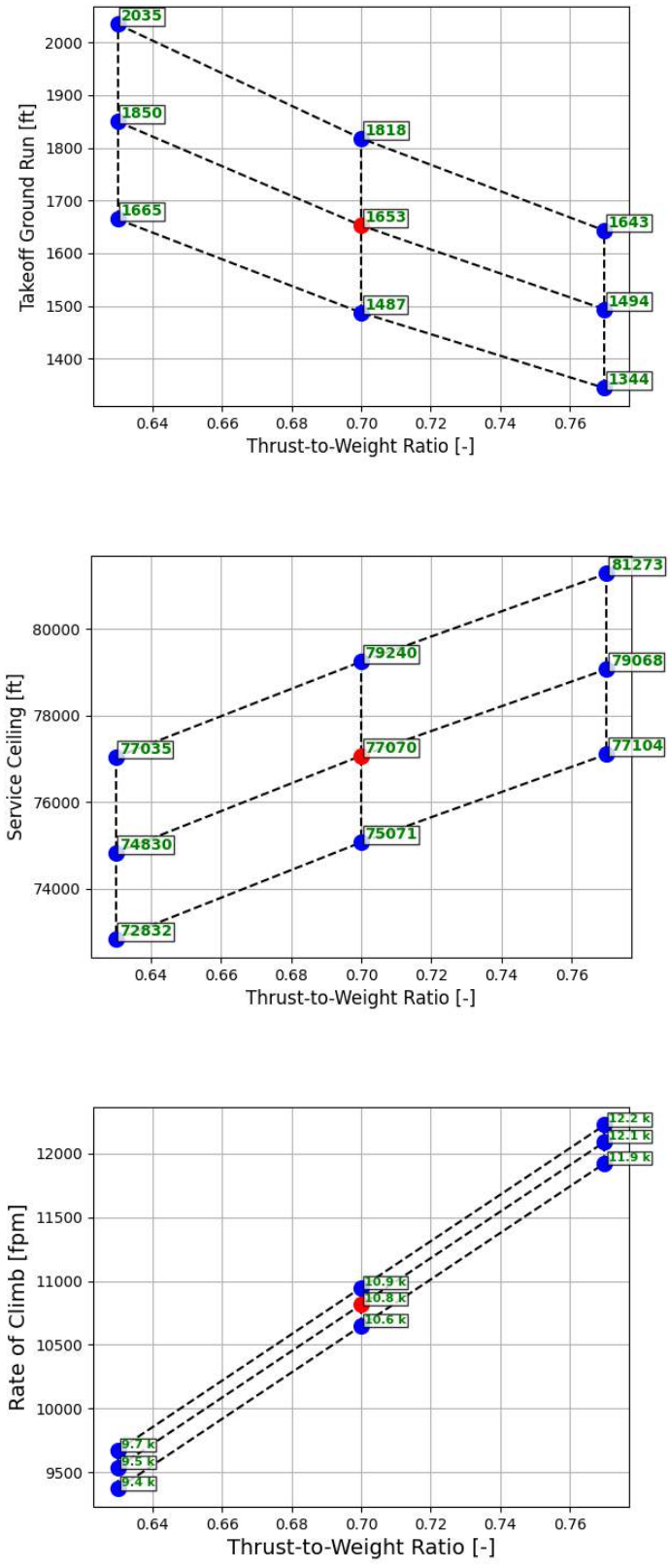

Figure 4-3: Baseline Parametric Trade Studies

The plots above were also generated with a module in *DSAeroTools*. Each marker indicates a combination of thrust-to-weight ratio and wing-loading. Red markers are the baseline design point of Table 2-2. The text label in green is the parameter being traded – takeoff ground run, service ceiling, or rate-of-climb.

The trade studies above indicate that the aircraft can comfortably meet the time-to-climb and takeoff requirements. It also indicates that the service ceiling is equally as sensitive to a 10% increase in thrust-to-weight ratio as it is to the same percent decrease in wing loading, an interesting result. Increasing the wing area is, in first order, favorable: the increase in thrust would require a significant increase in engine weight, whereas an increase in wing area comes at a structural weight cost though with the benefit of higher wing fuel volume.

4.4 Stall Speed – Cruise Speed Carpet Plot

A Stall Speed – Cruise Speed carpet plot was prepared for StratoSOL. This is particularly important to investigate the margin between cruise and stall speed at altitude, often referred to as the "coffin corner" for high-altitude and stratospheric aircraft. The plot is shown below:

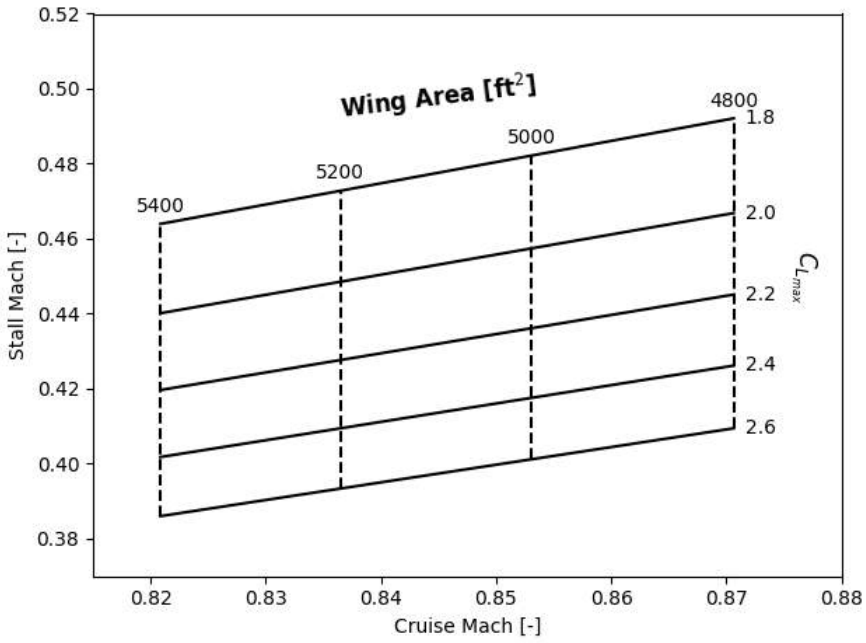

Figure 4-4: Stall-Cruise Mach Carpet Plot

And shows favorable margins between stall and cruise. This will be further investigated in performance analysis.

Chapter 5 – Configuration Downselect and Preliminary Layout

5.1 Configuration Downselect

To select a viable configuration for StratoSOL, a series of downselects were conducted. These are qualitative tradeoffs between different configurations based on key figures of merit (FoM). These downselects are shown below and include tables and figures to represent the different options considered.

5.1.1 Aircraft Configuration

Three aircraft configurations were traded: conventional, blended wing body (BWB), and hybrid wing body (HWB). A differentiation here is made between a BWB and HWB: the former has a singular lifting surface, that is, the lifting body and the fuselage are indistinguishable. The latter, however, has distinct lifting surfaces. The HWB may have a separate tail surface. The downselect is shown below:

Table 5-1: Aircraft Configuration Downselect

				
Figures of Merit	**Score Factor**	**Conventional**	**BWB**	**HWB**
Wetted Area	0.5	0	1	1
Stability & Control	0.3	0	-1	0
Manufacturing Complexity	0.2	0	-1	-1
	Total Score	**0**	**0**	**0.3**

Minimizing the wetted area is of great importance for the design point of StratoSOL, as was shown in the constraint analysis and mission profile analysis. Therefore, lifting fuselages are favorable for their reduced wetted area ratio, that is, the ratio between wetted and reference area. This comes with added challenges in the geometric layout of the aircraft.

Figure 5-1: NASA/Boeing X-48C

The most significant problem of a blended wing body is the lack of a longitudinal stabilizing surface, an issue addressed by careful selection of airfoils with trailing edge "cusps," which carefully tailor the pitching moment of the section. The problem can also be solved by a novel configuration layout: the installation of stabilizing surfaces at the rear of a lifting fuselage. This takes advantage of the reduced wetted area of lifting-fuselage configurations, while leaving more room for center of gravity shifts, important for a payload dispensing mission such as that of StratoSOL.

Lastly, manufacturing complexity was considered. State of the art composite manufacturing allows for feasible and cheaper lofts of complex, compound surfaces. There is also precedence in industry for the manufacturing of complex-shaped blended wing-style bodies. NASA and Boeing Phantom Works constructed three different models of an experimental blended/hybrid wing named the X-48[11]. Airbus has also worked on detailed concept designs of blended wing aircraft[12] and emerging startups such as JetZero[13] are currently developing similar models to be built and flown.

Figure 5-2: JetZero's Blended Wing Concept[13]

5.1.2 Tail Configuration

The selection of a hybrid wing body heavily constrains the selection of a tail configuration. Its placement is limited by the layout: aft, pod-mounted engines are favorable for stability and control, as well as to take full benefit of the aerodynamic efficiency of a lifting-fuselage by avoiding disturbances in the flow with wing-buried engines. Three options were considered, and the downselect is shown below:

Table 5-2: Tail Configuration Downselect

		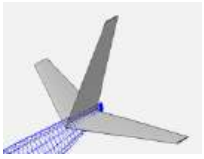	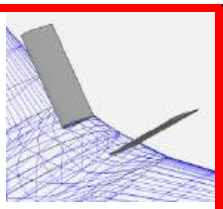	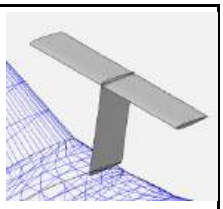
Figures of Merit	**Score Factor**	**Conventional**	**V-Tail**	**T-Tail**
Spin/Stall Recovery	0.5	0	1	1
Weight	0.3	0	0	-1
Complexity	0.2	0	-1	0
	Total Score	**0**	**0.3**	**0.2**

Conventional tails must be carefully laid out so that the elevator does not blanket the vertical stabilizer with separated flow at high angles of attack. This can make spin recovery practically impossible, and several general aviation aircraft have suffered from this issue[10]. V-Tails and T-Tails have their vertical surfaces clear of any wake, giving them a slight advantage.

T-Tails suffer from a slight penalty in weight. The placement of the horizontal stabilizer in a region that does not already have structural reinforcement (the top of the vertical stabilizer) adds to structural weight. Aircraft with conventional tails, on the other hand, already have structural reinforcement at the root of the vertical stabilizer for attachment with the fuselage, saving weight by structural synergy between the horizontal stabilizer and fuselage attachment. The same can be said about the placement of V-Tails. These tails also benefit from another advantage: because they are clear of the downwash of the wings, it gives them more margin for forward center of gravity placement while avoiding stalling the horizontal.

The downside of V-Tails is the added control complexity. The control surfaces act as both rudders and elevators, or *ruddervators*, and must be properly mixed to yield the correct controls. This can be achieved through a fly-by-wire system, and careful analysis into the dynamic behavior of the aircraft during critical stages of flight, particularly emergencies, such as stalls and spins.

5.1.3 Engine Placement

Lastly, the placement of the engines was considered. Three options were considered: aft pods, wing-buried, and underside. These are heavily constrained by operational and aerodynamic considerations. The downselect is shown below:

Table 5-3: Engine Placement Downselect

		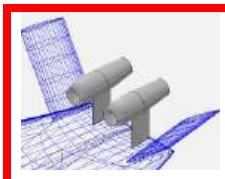	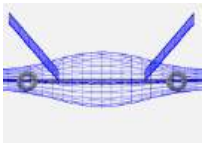	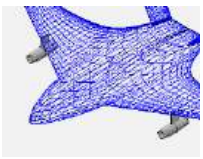
Figures of Merit	**Score Factor**	**Aft Pods**	**Wing Buried**	**Underside**
Aerodynamics	0.4	0	-1	0
Operational Considerations	0.4	0	-1	-1
Complexity	0.2	0	-1	0
	Total Score	**0**	**-1**	**-0.4**

Wing buried engines come with the cost of added drag from interference of the inlet-compressor and wing boundary layers. This also has implications for the operational capacity of the engine, and care must be taken in detailed analysis of the airfoil into the compressor at high angles-of-attack and in wing stall situations. Underside and aft-mounted engines are more common in several aircraft and, though they cannot avoid installation losses, they are less impacted by interference via careful placement and sizing of the pylons that mount the pods to the airframe.

Both underside and wing buried engines suffer from operational considerations, particularly in blended wing bodies. Wing buried engines are harder to access for much (and frequently) needed maintenance. This yields them impractical for a fleet of aircraft that must make round-the-clock flights. Underside mounted engines suffer from another operational consideration: ground clearance. Hybrid wing bodies have less clearance than a tubular-fuselage jetliner would, making higher mounted engines favorable.

Lastly, wing buried engines make for a more complex, difficult to manufacture airframe. There is also little precedent or research into the full implication – both in terms of the measures of merit discussed above as well as manufacturing – of wing buried engines in blended or hybrid wing bodies.

5.2 Blended Wing Geometry

5.2.1 Wing Sweep

Wing sweep increases the drag divergence Mach number, M_{dd}, by delaying the formation of shock waves in the wing's minimum pressure coefficient point, allowing aircraft to fly faster while remaining below the limit where wave drag grows exponentially. There is a strong correlation between the cruise Mach number and the wing sweep, as laid out in Raymer[10]. A preliminary sweep value is selected from this trend to be:

$$\Lambda_{LE} = 30°$$

5.2.2 Taper Ratio

A tapered planform creates a wing lift distribution closer to the ideal, elliptical distribution. This is particularly important in the case of aft-swept planforms: spanwise flow can promote tip-stall, so the planform must be tailored to avoid such phenomena and bring the maximum lift coefficient closer to the wing root[9, 10]. There is a strong correlation between the sweep angle and taper ratio. A preliminary value is chosen to be:

$$\lambda = 0.4$$

5.2.3 Wing Reference Area

The wing reference area can be calculated from the selected wing loading W/S and design takeoff gross weight W_0 values. It is calculated to be:

$$S_{ref} = 4{,}898 \text{ ft}^2$$

The reference area for a hybrid wing body includes the cabin or payload compartment, since the fuselage is a lifting body. However, its aerodynamic efficiency is diminished by the thicker boundary layer developed across its large-chord fuselage. Therefore, a correction factor is applied to the reference area to account for this fact, giving:

$$S_{ref_{corrected}} = 5{,}100 \text{ ft}^2$$

Of required lifting area. With the selected aspect ratio of 10, this yields the following geometry:

Table 5-4: Initial Weights

Parameter	Value
S_{ref}	5,100 ft^2
AR	10
Λ_{LE}	30°
b	225.8 ft
λ	0.4

5.2.4 Blended Wing Layout

The layout of the blended wing, including the cabin section as well as wing section, is shown in the figures below, and was conducted in OpenVSP[14]:

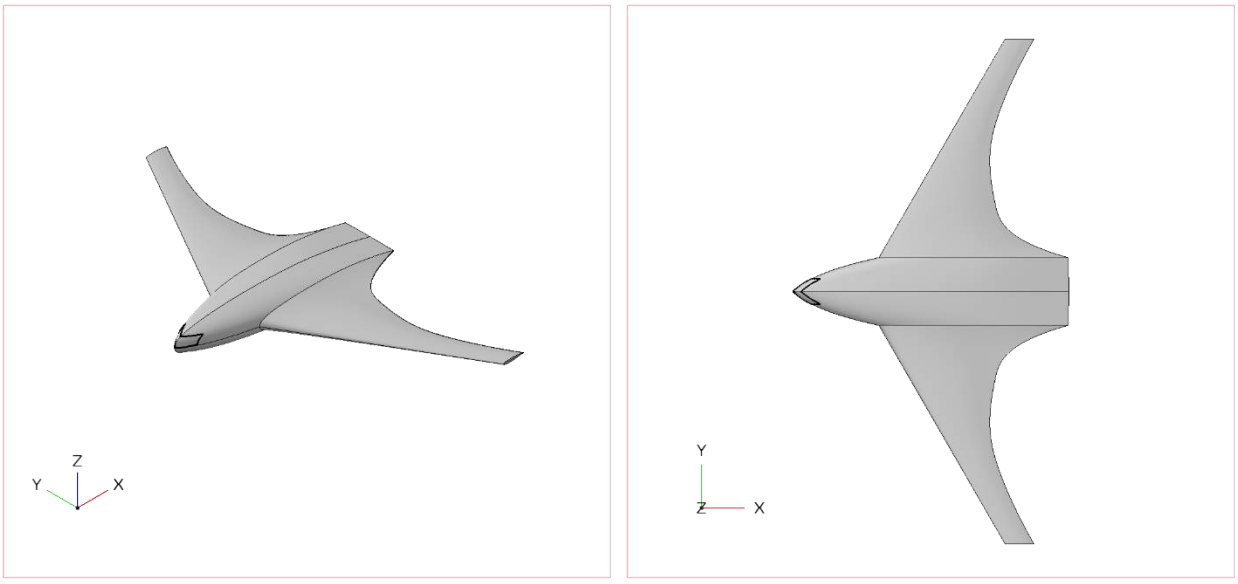

Figure 5-3: Preliminary Wing-Body Layout

5.3 Wing Airfoil

5.3.1 Introduction: Selection Considerations

Three main considerations guide the selection of an appropriate airfoil. Firstly, the airfoil's design lift coefficient must be determined. An airfoil with a high lift-to-drag ratio and minimal drag at said design lift coefficient is favorable. The sectional pitching moment coefficient must also be considered, though this is not a tailless aircraft so a negative pitching moment can be counteracted by the V-Tail in the aft section of the aircraft.

The critical Mach number of the section must also be considered. Though the aircraft may fly below supersonic speeds, the airfoil accelerates the flow over its surface, creating regions where the local Mach number is greater than that of the freestream. Therefore, an airfoil must be selected such that its local maximum Mach number remains below supersonic to avoid the formation of supersonic shocks in its surface.

Lastly, configuration considerations must be given to the selection. A low thickness airfoil is favorable to reduce compressibility and supersonic effects on drag but reduces the available space-claim for internal components. The wing thickness-to-chord ratio is constrained by the maximum fuel volume storage capability, while the payload compartment thickness-to-chord ratio is constrained by the available volume for the payload (aerosol tank) as well as aircraft systems (flight control, wiring, structural, etc.)

5.3.2 Design Lift Coefficient

The design lift coefficient is given by Equation (8):

$$C_l = \left(\frac{W}{S}\right)\frac{1}{q} = \left(\frac{W}{S}\right)\frac{2}{\rho V_{cr}^2} \tag{8}$$

And, for cruising flight at Mach 0.8 at 65,000ft, assumes the value of:

$$C_l = 0.61$$

Which is a very high cruising lift coefficient and will guide the selection of an appropriate airfoil. This also indicates the need for sophisticated high-lift devices during climb.

5.3.3 Internal Volume Requirements

The wing-body geometry is constrained by two main requirements: fuel and payloads.

The required fuel weight is found by the calculated fuel weight fraction and design takeoff gross weight. It is shown in Table 3-2. Therefore, the required fuel volume is found from the density of Jet A-1, tabulated in Raymer[10]. The required fuel volume is:

$$V_{fuel} = 865 \text{ ft}^3$$

The next constraint in internal volume is the payload. The RFP specifies 30,000lb of payload required per mission, and allows the assumption of the liquid density of the payload to be 15 lb/gal. This yields the following payload volume:

$$V_{payload} = 267 \text{ ft}^3$$

These requirements can be easily verified in OpenVSP. The software allows for the creation of a conformal geometry, which is a subgeometry of a major component (wing-body). By setting the density of the conformal object to 1, its mass becomes numerically equal to its volume, and the former can be computed within the software. Figure 5-4 shows two conformal geometries highlighted: internal wing volume, in green, and internal fuselage volume, in red. This procedure will be used to select an appropriate cross-section that satisfies all requirements above while minimizing compressible effects.

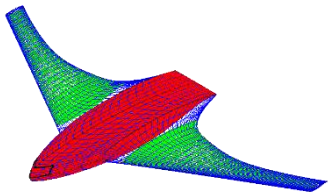

Figure 5-4: OpenVSP Conformal Geometry

5.3.4 Estimation of Mach Divergence

A key consideration for wing airfoil selection is the drag-divergence Mach number, M_{dd}. There are two widely accepted definitions for the drag-divergence Mach number. By Boeing's definition, this is the Mach number at which the wave drag coefficient reaches 20 counts (0.002). By Douglas' definition, this is the Mach number at which the slope of the wave drag coefficient versus Mach number reaches 0.1, that is, the wave drag coefficient is rising by 1000 counts for each unit increase in Mach.

The drag-divergence Mach number for an airfoil, M_{dd}, is typically $M_{dd} \approx 1.02\, M_{crit}$[9]. It can be estimated using Korn's Relation[15], shown in Equation (9):

$$\kappa - t/c - 0.1 C_{l_{design}} \tag{9}$$

Where κ is a constant obtained through CFD analysis, and Gudmundsson[9] recommends a value of 0.95 for NASA-style supercritical airfoils; t/c is the airfoil's thickness-to-chord ratio, and $C_{l_{design}}$ is the airfoil's design lift coefficient.

A few candidate airfoils, all NASA Supercritical Airfoils, were analyzed. Table 5-5 shows the airfoil's available wing fuel volume obtained in OpenVSP, as well as whether there is enough internal volume for payload and components:

Table 5-5: Candidate Airfoils

Airfoil	$C_{l_{design}}$	t/c	M_{dd}	Wing Volume [ft^3]	Fuselage Volume [ft^3]	Enough Internal Volume [Y / N]
SC(2)-0614	0.6	14%	0.75	2760	8288	Y
SC(2)-0610	0.6	10%	0.79	1918	5904	Y
SC(2)-0606	0.6	6%	0.83	1062	3472	Y
SC(2)-0414	0.4	14%	0.77	2764	8302	Y
SC(2)-0410	0.4	10%	0.81	1919	5906	Y
SC(2)-0406	0.4	6%	0.85	1070	3495	Y

The airfoils were also analyzed in XFOIL[16] for their performance in the design cruise conditions. Their lift and drag polars are shown below, at a Reynold's Number of $1.62 \cdot 10^7$:

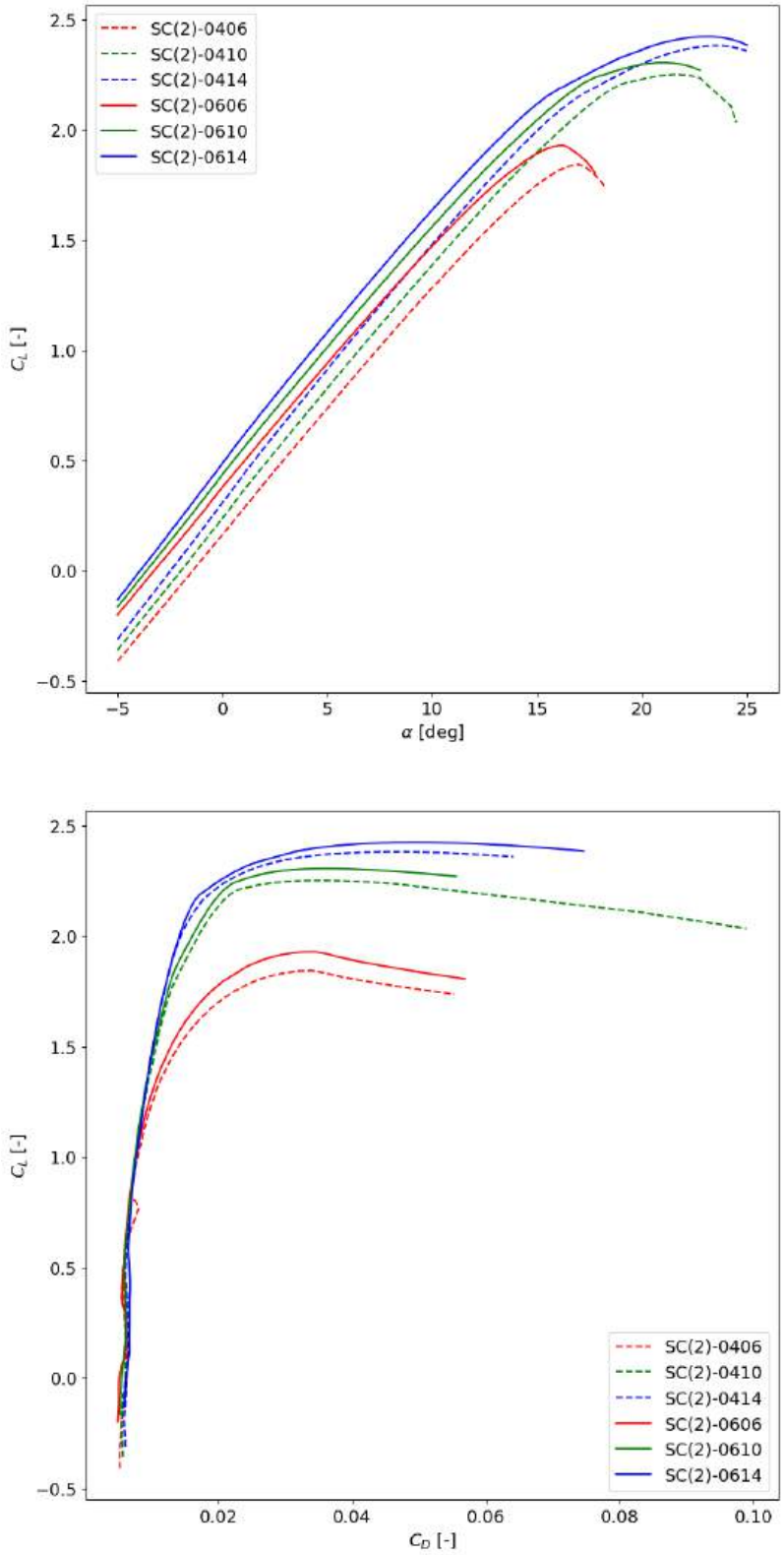

Figure 5-5: Airfoil Candidate Polars

In the polars above, each color represents a thickness, and dotted lines represent airfoils of lower design lift coefficient. The drag difference at the design lift coefficient between airfoils of different thickness and design lift coefficient is negligible: 5 counts at max. Therefore, the main constraint on the airfoil is the increase in M_{dd} as well as sufficient internal volume for layout.

All airfoils satisfy the internal volume and fuel requirements. Thinner airfoils are preferred for high-speed flight, as evidenced by their higher drag-divergence Mach numbers. The 14% thickness SC(2)-0614 is preferred for the wing-body since it allows ample room for the aerosol tank as well as other space-claim components such as landing-gear, flight control systems, and APU. The thinner SC(2)-0610 and SC(2)-0406 are preferred for the wing geometry. The outboard airfoil has a lower design lift coefficient since the outboard sections fly at reduced lift coefficients from the drop in lift distribution. The selected airfoils are thus shown in Table 5-6: Selected Airfoils:

Table 5-6: Selected Airfoils

Location	Airfoil	
Wing-Body Root	SC(2)-0614	
Wing-Body Tip	SC(2)-0610	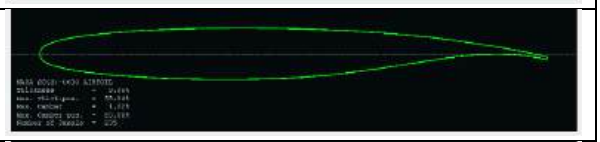
Wing Tip	SC(2)-0406	

5.4 Tail Sizing

The tail sizing procedure for V-Tails is similar to that of conventional tails. This author will use the method of tail volume coefficients. Of course, there is no vertical and horizontal surface since each V-Tail acts in both longitudinal and lateral-directional stability and control. However, for the purpose of sizing, the surface area of an equivalent pair of horizontal and vertical must each be determined. Therefore, these will be referred to as equivalent surface areas, and are used to size the V-surfaces.

The horizontal and vertical tail areas can be written in terms of volume coefficients as defined by Equations *(10)* and *(11)*:

$$S_H = \frac{V_H \overline{C_W} S_W}{L_H} \tag{10}$$

$$S_V = \frac{V_V b_W S_W}{L_V} \tag{11}$$

Where V_H and V_V are the horizontal and vertical tail volume coefficients, respectively. These are selected for aircraft of similar weight range[9, 11] and are, respectively, 0.9 and 0.07. The horizontal and vertical moment arms, L_H and L_V, are set by the geometry of the aircraft and are estimated in OpenVSP to be $L_H = L_V \approx 46$ ft. The sizing for the moment arm was iterative: the tail was laid out and its moment arm verified, followed by the required areas. Unreasonably large tails were cut shorter by increasing their sweep, and thus the moment arm. For the sizing, an equivalent planform was used. Its geometry as well as the calculated moment arm are shown in Figure 5-6:

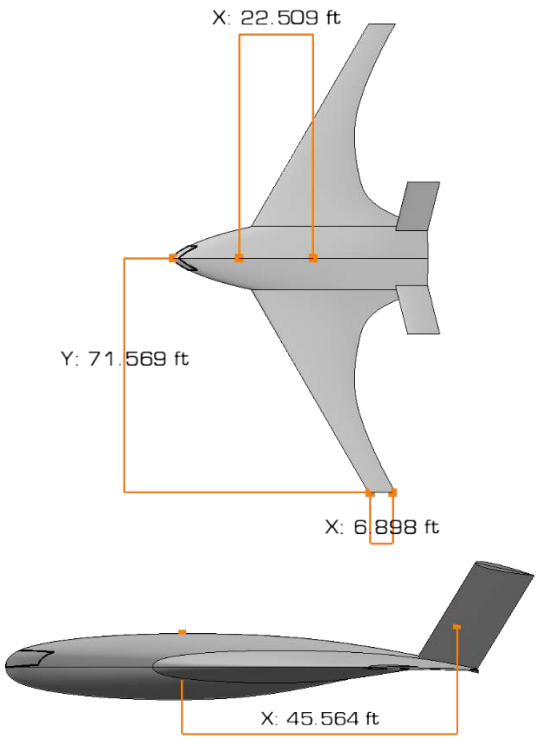

Figure 5-6: Equivalent Planform and Tail Sizing Geometry

The equivalent horizontal and vertical areas are therefore calculated to be:

$$S_H = 332 \text{ ft}^2$$

$$S_V = 115 \text{ ft}^2$$

Per Purser and Campbell[17], the V-Surfaces are sized to have same total surface area as the equivalent horizontal-vertical pair. The dihedral angle Γ of the V-Surface is given by Equation *(12)*:

$$\Gamma = \tan^{-1}\left(\sqrt{\frac{S_V}{S_H}}\right) \tag{12}$$

And is determined to be 30.5°.

5.5 Preliminary Layout

A four-view of the finalized preliminary layout is shown in Figure 5-7:

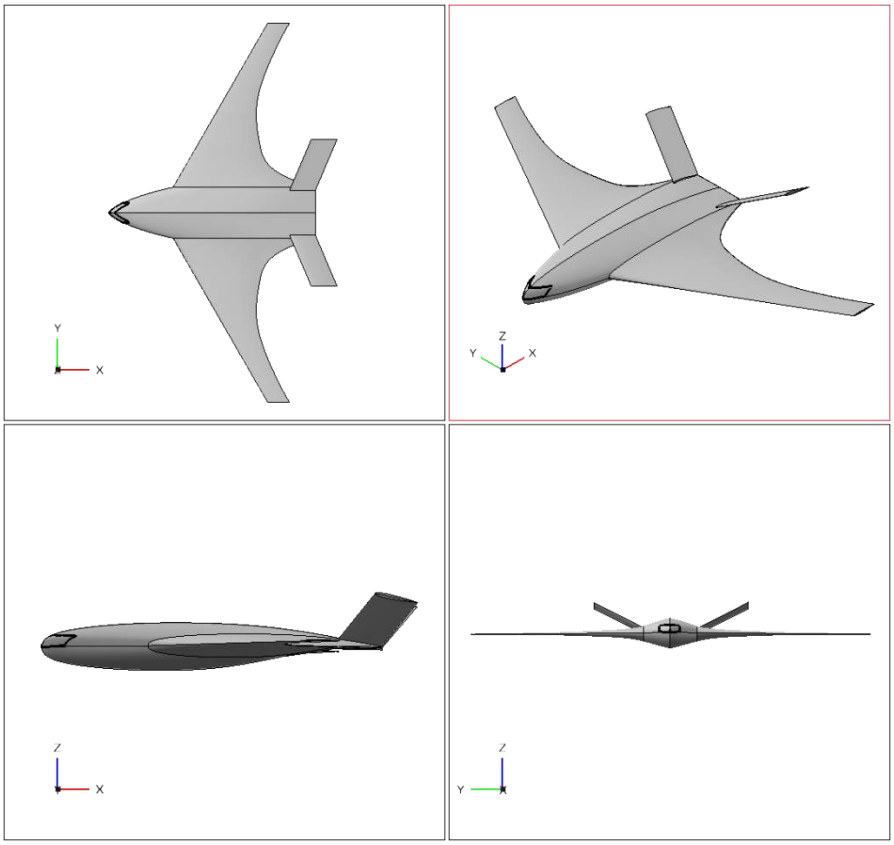

Figure 5-7: Final Preliminary Layout

Chapter 6 – Weight Analysis and Revised Layout

6.1 Powerplant: Overview and Selection

Prior to Class I weight estimates, a preliminary engine selection must be made to estimate its weight and effect on the center of gravity. The required thrust is calculated from the selected thrust-to-weight ratio from constraint analysis and the design takeoff gross weight. It is calculated to be:

$$T_0 = 120{,}000\ lb_f$$

Two primary aspects of StratoSOL's design point constrain its engine selection heavily: its high operating altitude of 65,000' as well as its high cruise speeds of upwards of Mach 0.7-0.8. The selected engine must be capable of climbing to altitude, maintaining level flight at the altitude, and cruise at the desired transonic speeds. Figure 6-1 shows the typical flight envelope – altitude versus velocity – of different engine types:

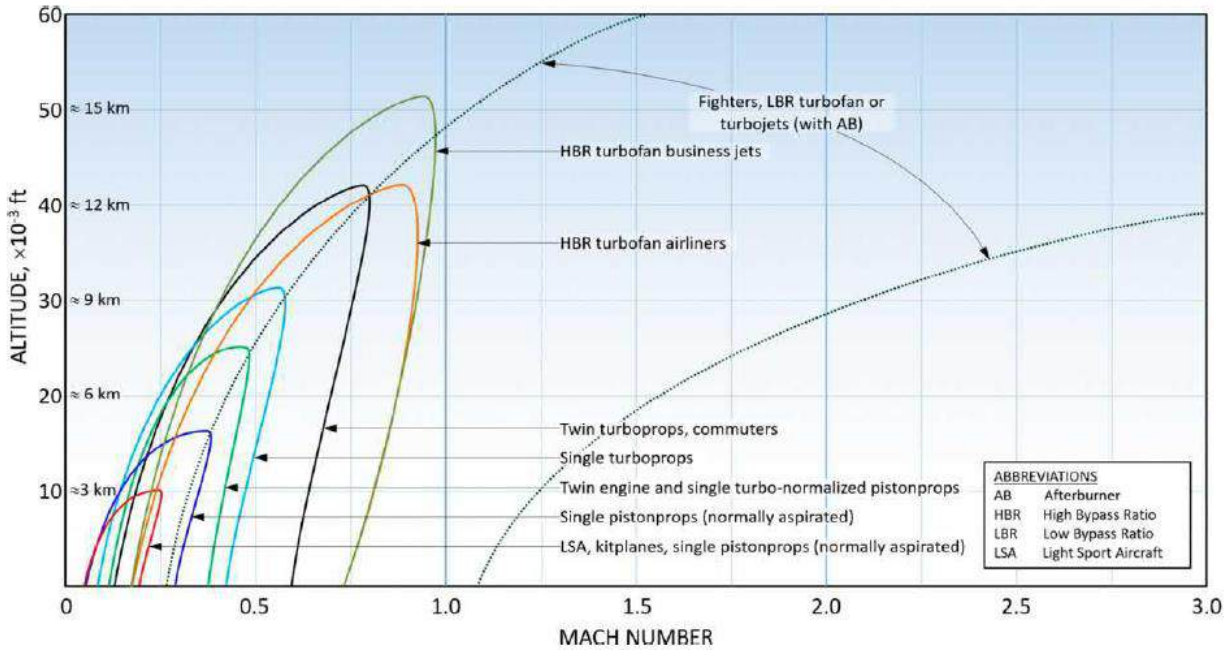

Figure 6-1: Typical Flight Envelope of Engine Types (from Gudmundsson's General Aviation Aircraft Design[9])

At the desired cruise Mach speeds of StratoSOL, turbofans are favorable. The challenge is to find a turbofan, ideally with a high bypass-ratio for fuel efficiency, that is also able to operate at high altitudes. The reason is related to the thermodynamic cycle design, as explained in [18]: high bypass ratio engines achieve supersonic turbine tip Mach speeds, in the order of Mach 1.3. This causes tip losses in the turbines, but these losses are more than made-up for by increasing the overall pressure ratio towards the center of the turbine upstream of the compressor, increasing the core's thermal efficiency. However, as altitude increases, the local Reynold's numbers decrease, and the supersonic tip losses grow exponentially more significant. The thrust drops significantly with increasing altitudes, rendering altitude effects crucial for the design point of StratoSOL.

A compromise must be made for a stratospheric lofter aircraft. A number of engines were investigated with three primary concerns in mind: rated thrust, integration, and efficiency. Although previously used high-altitude platforms such as the U2's F118-GE-101 are good candidates, they do not provide sufficient thrust needed by the high thrust-to-weight ratio application at hand. Their use in a 170,000 lb aircraft would require 6 or 7 engines, which is impractical for installation in a HWB configuration. A compromise is made with a higher thrust-rating family. The RB211-524H-T was therefore selected. The engine, along with its specifications, are shown in Figure 6-2 and Table 6-1:

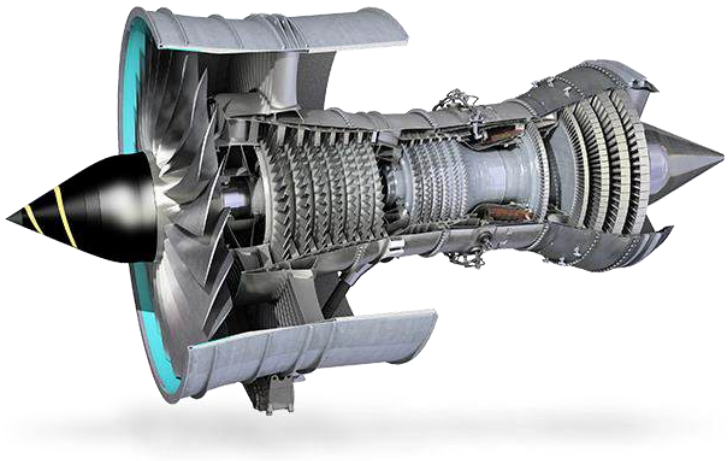

Figure 6-2: RB211-524H-T (Source: Rolls Royce[19])

Table 6-1: RB211-524H-T Specifications[20]

Parameter	Value
Rated SL Thrust	60,600 lb
Weight	9,470 lb
Nominal Length	10.4 ft
Nominal Diameter	7.2 ft
Max Power OPR	34:1

The RB211-524H-T engines offers a perfect combination of small enough outer mold line dimensions and thrust rating. At 60,600 lb, StratoSOL requires only 2 engines to operate at the design cruising altitude of 65,000 ft. These engines are small enough to be integrated toward the aft section of the aircraft's wing-body fuselage. This would not be possible with the newer generation F118's: they would simply require too many engines to install in the configuration. The downside is that the F118-GE-100 and -101 series of engines are designed for gained efficiency at high-altitude flight. They incorporate careful aerodynamic design of the fan blades to yield reduced supersonic tip losses, increasing the efficiency. Although Rolls Royce's series does not have such upgrades, they have proven themselves in Boeing's 747 and 767 wide-body aircraft. The aircraft are reported to have flown well beyond their expected flight envelopes, and its engines have notoriety for their high performance. However, this warrants further investigation. Ideally, the development of a new, 40,000-60,000 lb rated engine with aerodynamic and thermodynamic design for flight at stratospheric altitudes would enable a new generation of reconnaissance aircraft that takes advantage of sleek configuration design with the reduced OML space-claim requirements of such new engine. The cost analysis will explore the economic effects of the development of said platform. A preliminary integration of the engines is shown in Figure 6-3:

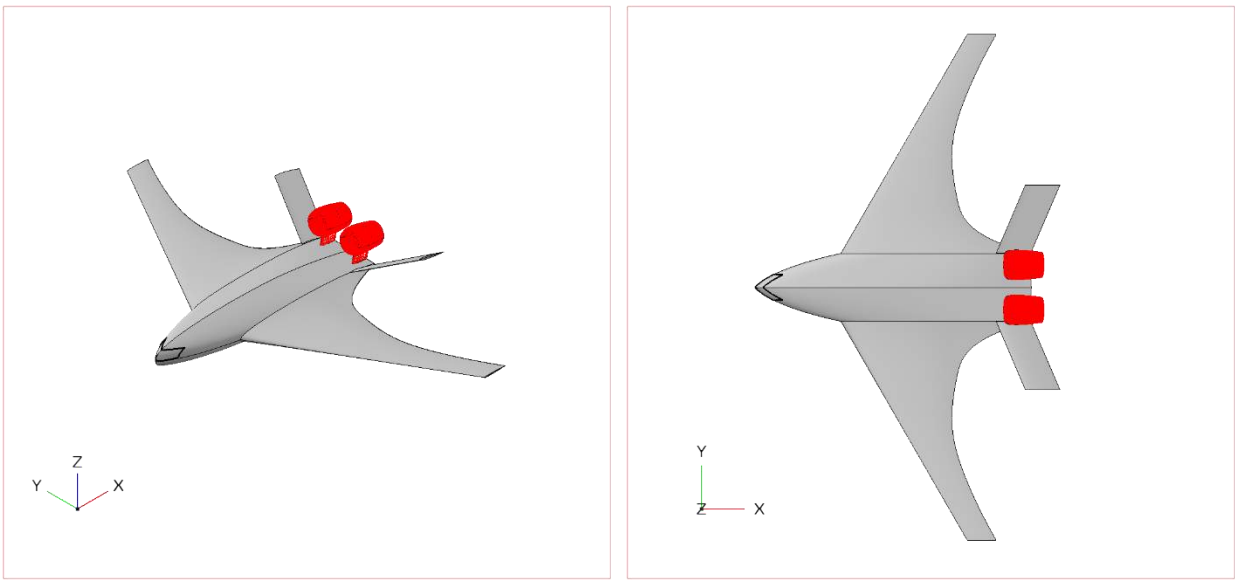

Figure 6-3: Preliminary Engine Integration

6.2 Class I Weight Analysis

An initial estimate of empty weight is made using Class I methods for weight analysis. These methods involve the use of simple weight fractions from aircraft of similar class to provide an initial basic weight group statement. Methods in Roskam[21] and Raymer[10] are used below.

Table 6-2 is adapted from Roskam[21], with the maximum takeoff gross weight (MTOW) added to show proximity to StratoSOL's design takeoff weight. It shows several weight group fractions, each including the weight of different subsystems associated with the group:

Table 6-2: Roskam's Class I Weight Fractions

Aircraft	$MTOW$ [lb]	$\frac{W_{powerplant}}{W_0}$	$\frac{W_{fixed\ eq}}{W_0}$	$\frac{W_{wing}}{W_0}$	$\frac{W_{empenage}}{W_0}$	$\frac{W_{fuselage}}{W_0}$	$\frac{W_{gears}}{W_0}$
McDonnel-Douglas DC-9-30	157,000	0.076	0.175	0.106	0.026	0.103	0.039
McDonnel-Douglas MD-80	161,000	0.079	0.182	0.111	0.024	0.115	0.038
Boeing 737-200	139,000	0.071	0.129	0.092	0.024	0.105	0.038
Boeing 727-100	160,000	0.078	0.133	0.111	0.026	0.111	0.045
Average	154,000	0.076	0.155	0.105	0.025	0.109	0.04

The powerplant group includes the engines themselves (as well as thrust reversers, if applicable), air induction systems, fuel systems, and any auxiliary propulsion-related systems contained in the cowling or nacelle. The fixed-equipment group is quite comprehensive and accounts for several subsystems fixed in the airframe, including flight control systems, hydraulic and pneumatic systems, electrical systems, avionics, air conditioning, APU, furnishings, and operational items. The wing, empennage, and fuselage weight groups include the structural weight of the components. Finally, the landing gear group includes the structural weight of the tires and wheel-assembly. Raymer suggests attributing 15% of the weight of the gears group to the nose gear, and the rest to the mains.

Raymer[10] suggests a similar approach, but provides averaged data for aircraft of similar class referencing not simply the design takeoff weight but also relevant geometric parameters for each weight group. Table 6-3 is adapted from the author in question, and shows weight fractions:

Table 6-3: Raymer's Class I Weight Fractions (Transport & Bomber)

Weight Group	Weight Fraction	Reference Parameter
Powerplant	1.3	Engine Weight
Fixed Equipment	0.17	MTOW
Wing	10 lb/ft^2	Exposed Planform Area
Empennage	5.5 lb/ft^2	Exposed Planform Area
Fuselage	5 lb/ft^2	Wetted Area
Gears	0.043	MTOW

The weight groups above are similar to Roskam's. Both methods can be used to arrive at a first estimate of the empty weight and center of gravity. To design for stability, an initial estimate of the neutral point is also useful. A preliminary XFLR5[22] model of the lifting surfaces was created, shown in Figure 6-4:

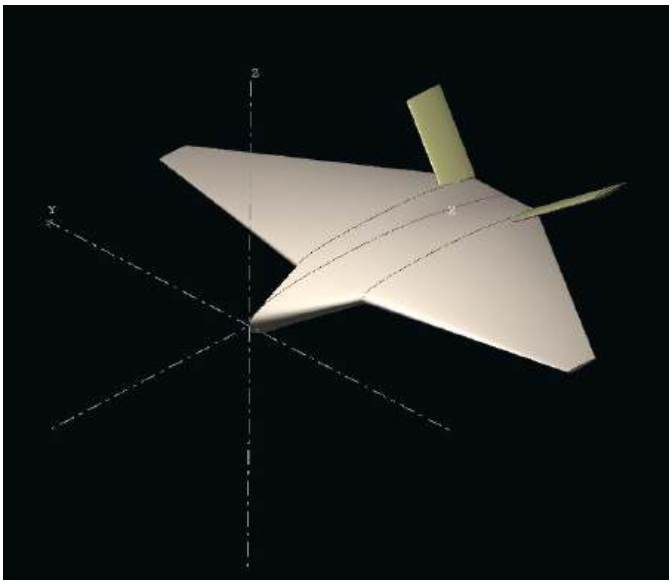

Figure 6-4: StratoSOL XFLR5 Model

From this model, a vortex-lattice solver is run, and several parameters estimated. Notably, a first estimate of the neutral point is found to be:

$$X_{NP} \approx 49 \text{ ft}$$

And can be used for a first-order placement of the subsystems using the Class I methods. Table 6-4 shows the computed weight groups along with a first-order placement. A first guess of the engine weight was made based on aircraft of appropriate thrust-rating, as detailed in section 6.1. The selected *datum* is the nose of the wing-body (the leading edge of the root wing-body airfoil):

Table 6-4: Class I Weight Groups

Weight Group	Roskam	Raymer
Powerplant [lb]	13,029	24,622
Fixed Equipment [lb]	26,573	29,145
Wing [lb]	18,001	10,540
Empennage [lb]	4,286	4,914
Fuselage [lb]	18,687	20,230
Main Gear [lb]	5,829	6,266
Nose Gear [lb]	1,029	1,106
Total Empty	87,434 lb	96,822 lb

Although neither method agrees well with the statistical empty weight, Raymer's method is in good agreement with the design takeoff gross weight, within a percent when the fuel weight, crew weight, and payload weight are added to the calculated 96,800 lb empty weight. The following longitudinal distribution, shown in Table 6-5, yields a statically stable aircraft in all flight configurations, as will be shown in the CG excursion diagram:

Table 6-5: Class I Weight Distribution

Weight Group	Xloc [ft]
Powerplant	73.0
Fixed Equipment	30.0
Wing	42.6
Empennage	73.0
Fuselage	42.6
Main Gear	50.0
Nose Gear	10.0
Payload	45.0
Crew	8.0
Fuel	42.6
CG Location [ft]	46.0
Static Margin [% MAC]	14.4

6.3 Class II Weight Analysis

Class II weight analysis was conducted using a collection of Class II methods, inspired by the methodology in [23]. These are statistical models for the weights of several different components and subsystems of the aircraft. Class II methods allow for a more precise estimation of the empty weight of the aircraft divided into a weight group statement.

Equations *(13)* through *(26)* give the mass of several components of the aircraft:

$$m_{cabin} = 0.316422\left(\frac{5.698865}{450}n_{pax}\right)(W_0)^{0.166552}(S_{cabin})^{1.0161158} \quad (13)$$

$$m_{aft} = 0.53(1 + 0.05n_{eng})(S_{aft})(W_0)^{0.2}(\lambda_{aft} + 0.5) \quad (14)$$

$$m_{wo} = 0.8c_1\left[\left(\frac{b_s}{\cos\Lambda_{0.25}}\right)\left(\frac{1+2\lambda}{3+3\lambda}\right)\left(\frac{W_0 n}{s}\right)^{0.3}\left(\frac{v_D}{\tau}\right)^{0.5}\right]^{0.9} \quad (15)$$

$$m_{LG} = 0.0445W_0 \quad (16)$$

$$n_{nacelle} = 0.055T_{TO}n_{eng} \quad (17)$$

$$m_{APU} = 0.001W_0 \quad (18)$$

$$m_{engine\ inst} = n_{eng}\left(5 + \frac{0.0132276W_0}{1000}\right) \quad (19)$$

$$m_{flight\ inst} = 2\left(15 + \frac{0.0705472W_0}{1000}\right) \quad (20)$$

$$m_{other\ inst} = \frac{0.33069W_0}{1000} + 0.0264552W_0 \quad (21)$$

$$m_{inst} = 0.4536(m_{engine\ inst} + m_{flight\ inst} + m_{other\ inst}) \quad (22)$$

$$m_{hydr} = 3.2W_0^{0.5} \quad (23)$$

$$m_{AC} = 10.045l_{cab}^{1.28} \quad (24)$$

$$m_{elec} = 0.75W_0^{0.67} \quad (25)$$

$$m_{flight\ controls} = 0.11W_0^{0.8} \quad (26)$$

And Table 6-6 describes each equation, its meaning, and its authors:

Table 6-6: Class II Method Equations

Mass	Description	Auhtor(s)
m_{cabin}	Wing-Body Fuselage Mass	Bradley[24]
m_{aft}	Wing-Body Aft Section Mass	Bradley
m_{wo}	Outer Wing-Body Mass	Howe[25]
m_{LG}	Landing Gear Mass	Jenkinson[26]
$n_{nacelle}$	Engine Nacelle Mass	Torenbeek[27]
m_{APU}	Auxiliary Power Unit Mass	Kundu[28]
$m_{engine\ inst}$	Engine-Related Instrumentation Mass	Roskam
$m_{flight\ inst}$	Flight-Related Instrumentation Mass	Roskam
$m_{other\ inst}$	Miscellaneous Instrumentation Mass	Roskam
m_{inst}	Installed Instrumentation Mass	Roskam
m_{hydr}	Hydraulic Mass	Cranfield[23]
m_{AC}	Air-Conditioning Mass	Torenbeek
m_{elec}	Electrical Mass	Cranfield[23]
$m_{flight\ controls}$	Flight Controls Mass	Cranfield[23]

It is worth noting that some of the expressions above were adapted to better fit the mission in hand. For instance, the equation for the cabin mass includes the number of passengers. This is because the equation was developed for Boeing's BWB studies for a blended wing body commercial transport. In this case, this author investigated how many passengers StratoSOL would have been able to carry within its cabin, and used that number for the computations.

These values were computed and are shown in the final group weight statement in Table 6-7:

Table 6-7: StratoSOL Class II Group Weight Statement

Component	Weight [lb]
Wing-Body Fuselage	12,725
Wing-Body Aft	2,356
Wing-Body Outer Wing	20,461
Nose Gear	1,144
Main Gear	6,485
Nacelle	13,201
Empennage	4,914
APU	171
Installed Instruments	4,710
Installed Engines	24,622
Hydraulics	1,325
Air Conditioning	4,725
Electrical	2,409
Flight Controls	1,693
Payload	30,000
Fuel	43,333
Total	**171,728**

6.4 CG Excursion Diagram

Using the weight analysis above, a CG excursion diagram was prepared. It shows that the aircraft can maintain its static margin within the forward and aft limits in all configurations with exception of the empty weight without the crew and their luggage. This is not a problem since the aircraft cannot operate in that configuration. The excursion diagram is shown in Figure 6-5:

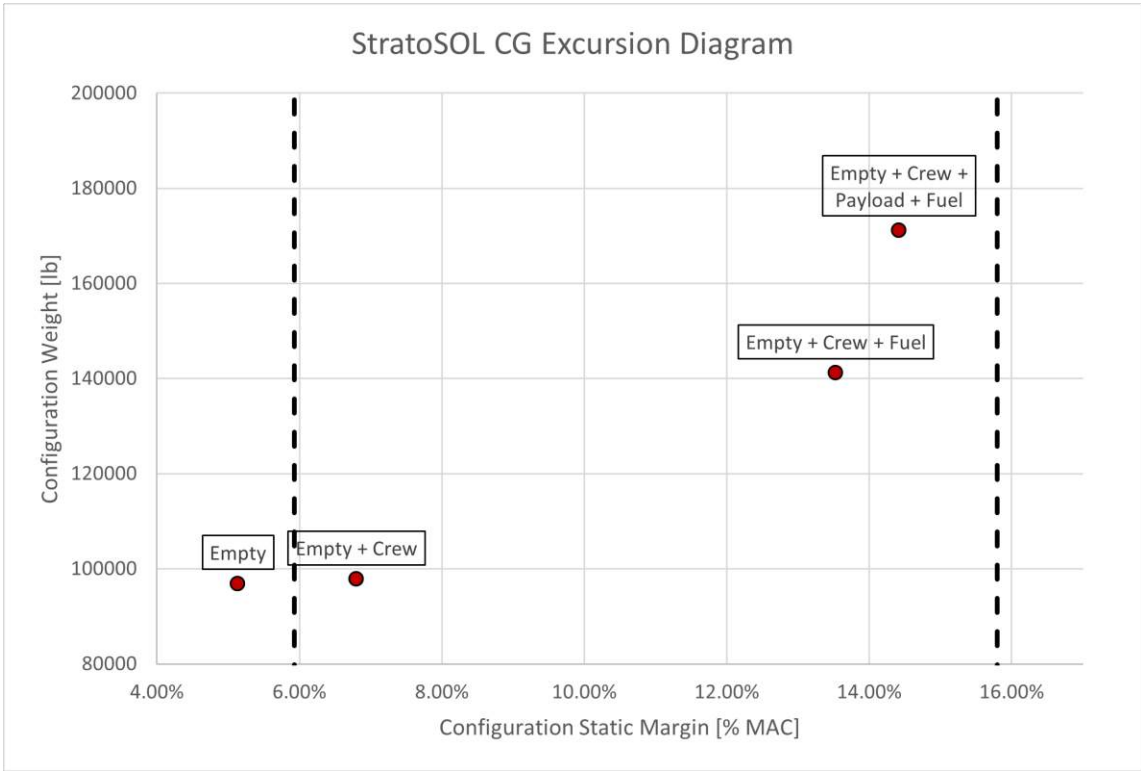

Figure 6-5: StratoSOL CG Excursion Diagram

It is also worth noting that although the empty aircraft lies outside the CG Envelope, the landing gears are laid out such that the aircraft does not tip over its tail. The sizing and layout of the landing gear is shown in the following section.

6.5 Landing Gear Sizing

Before the revised layout, sizing of the landing gears must be performed. Raymer provides a statistical first-order model to size the landing gears based on historical weights. The diameter and width of the gears can be found with Equations *(27)* and *(28)*:

$$d = 1.63 W_W^{0.315} \tag{27}$$

$$w = 0.1043 W_W^{0.48} \tag{28}$$

Where W_W is the weight carried by each wheel. At first order, it can be assumed that the nose wheel assumes 60-100% of the linear dimensions of the main wheels. Additionally, it can be assumed that the main wheels bear 90% of the weight of the aircraft, and the nose wheels bear the remaining 10%. Lastly, note that "wheels" mean the entire oleo-pneumatic assembly, not just the tires. This is useful for space-claim purposes in the revised layout.

With 4 tires in each main wheel and 2 tires in the nose wheel, this yields the following dimensions:

$$d = 3.0 \text{ ft}$$

$$w = 1 \text{ ft}$$

And a top view of the landing gear geometry in its tricycle configuration is shown in Figure 6-6:

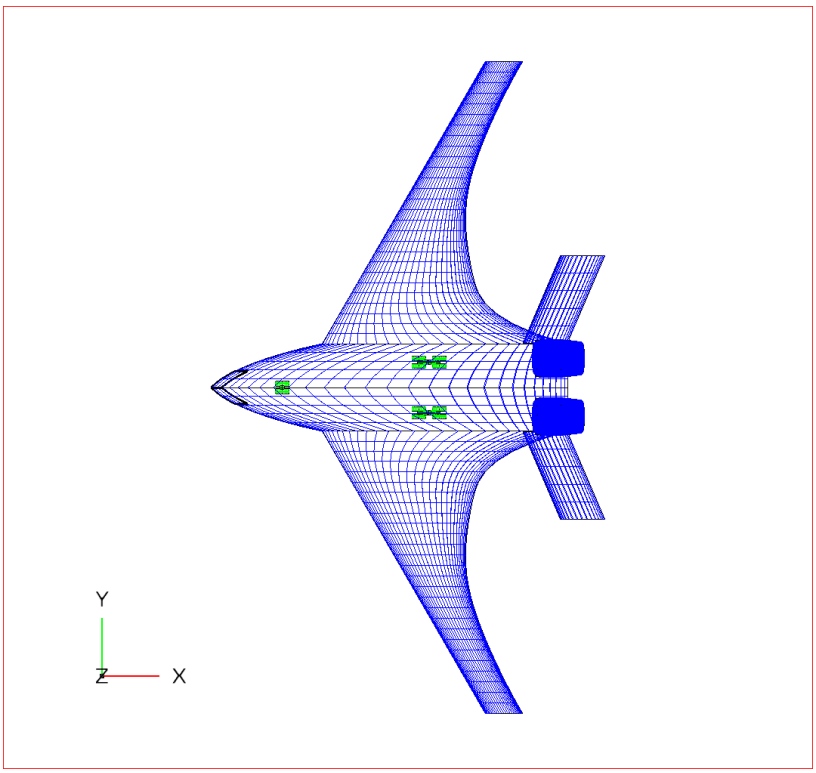

Figure 6-6: Landing Gear Layout

6.6 Revised Layout

6.6.1 Fuel System

StratoSOL holds the fuel required for its design mission in its wet-wing. The required fuel volume was calculated before to be:

$$V_{fuel} = 865 \text{ ft}^3$$

The fuel tanks were laid out in OpenVSP until the desired volume was achieved. The fuel system layout is shown in Figure 6-7:

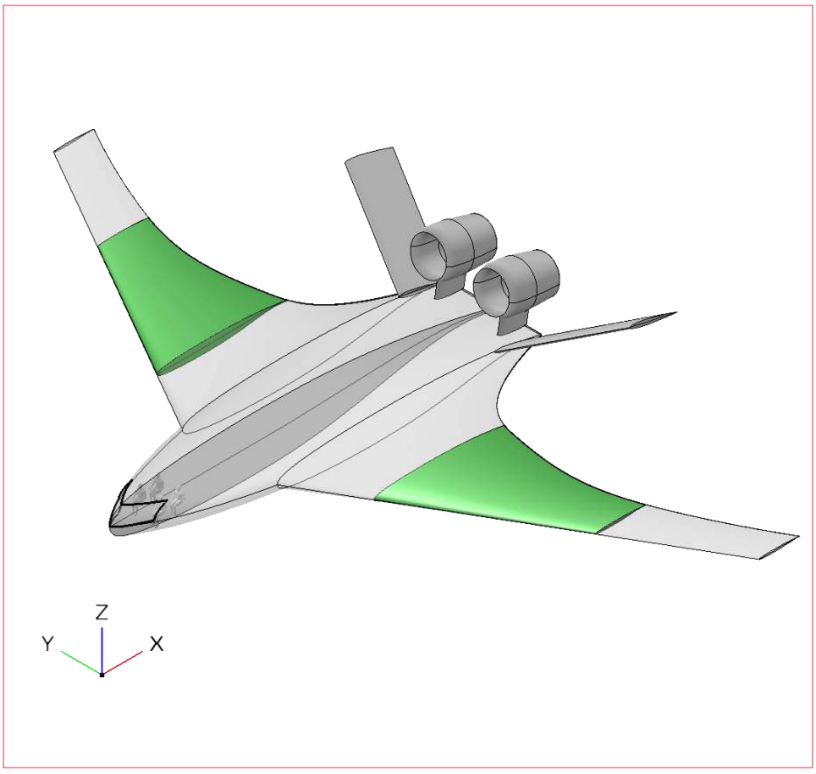

Figure 6-7: Fuel Tank System

6.6.2 Aerosol Tank and Injection System

To hold 30,000 lb of aerosol, the tank must have an internal volume of:

$$V_{aerosol} = 267 \text{ ft}^3$$

In case the aerosol is a pressurized vessel, it was laid out in the shape of a pressure vessel. Its small dimensions work well with the configuration of the aircraft: in its designated CG location, it sits in the middle of the fuselage in between the two main gears, which are retracted beside it. An isometric view of the tank as well as its configuration within the aircraft is shown in the figures below:

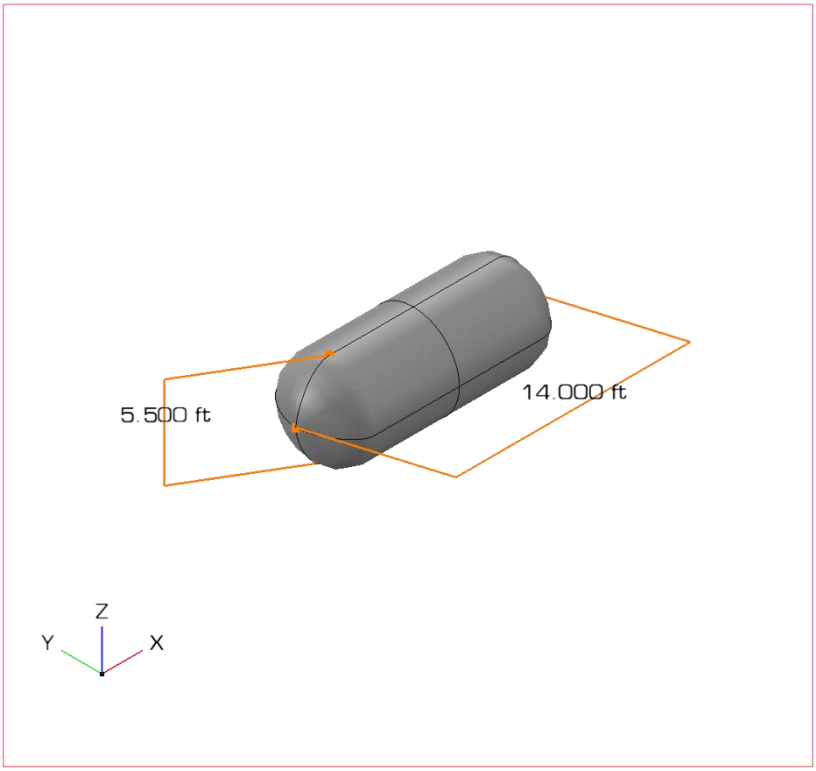

Figure 6-8: Aerosol Tank Geometry and Dimensions

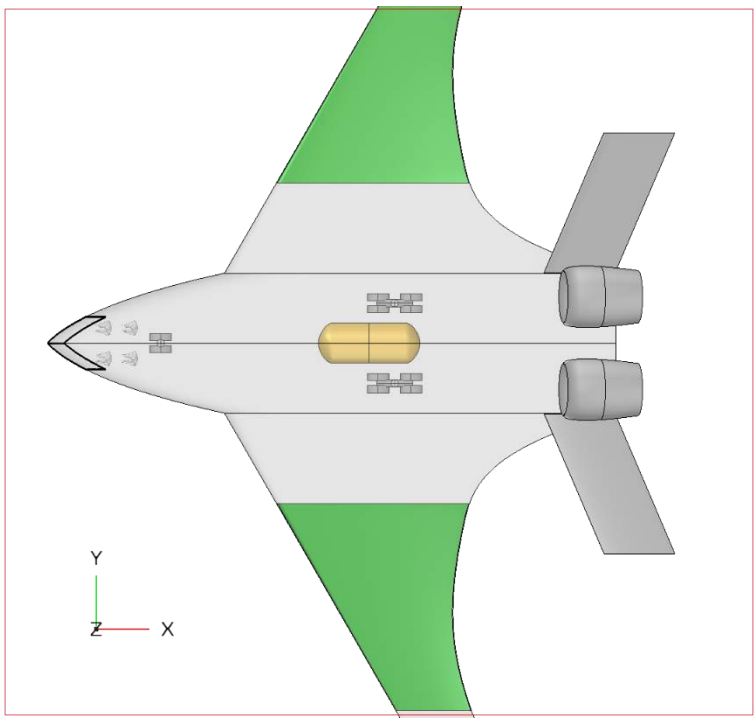

Figure 6-9: Aerosol Tank Configuration (Top)

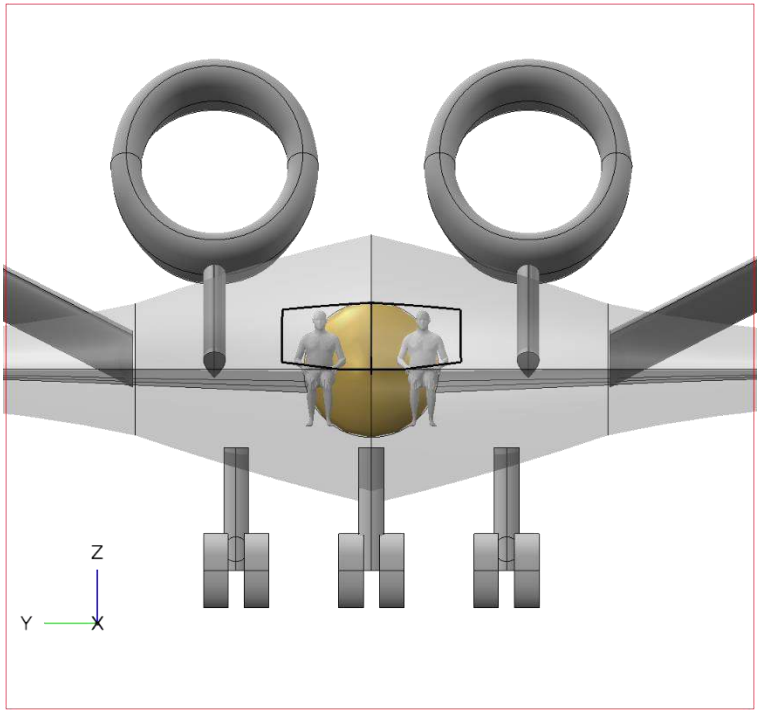

Figure 6-10: Aerosol Tank Configuration (Front)

During nominal operation, the tank will release the aerosol particles from underneath the fuselage. Four nozzles will extend from the bottom of the tank, in addition to a filling valve port. This allows for easy loading and venting of the aerosol in ground operations. A bottom view of the release system is shown in Figure 6-11:

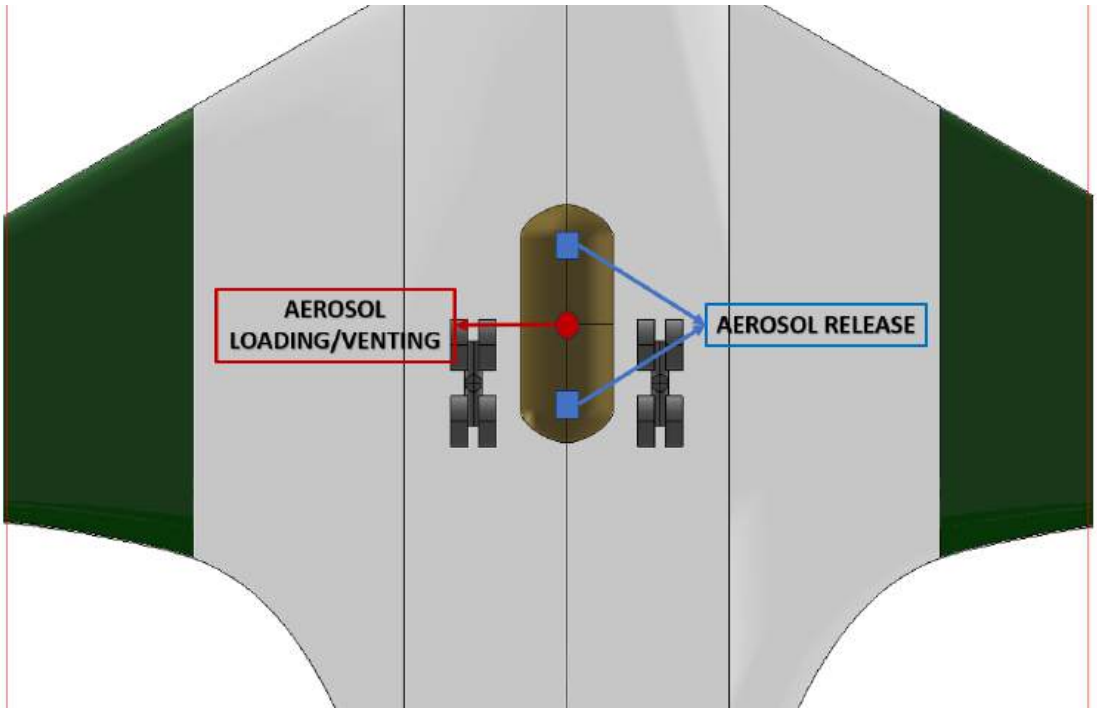

Figure 6-11: Aerosol Tank Loading/Venting System

6.6.3 Four View and Rotation Clearance

Below is a four of the final layout of StratoSOL. Shown are the gears deployed configuration. Highlighted in the wing are the fuel tanks, and the aerosol tanks and landing gears are visible in the fuselage. The figure below also shows the available rotation angle:

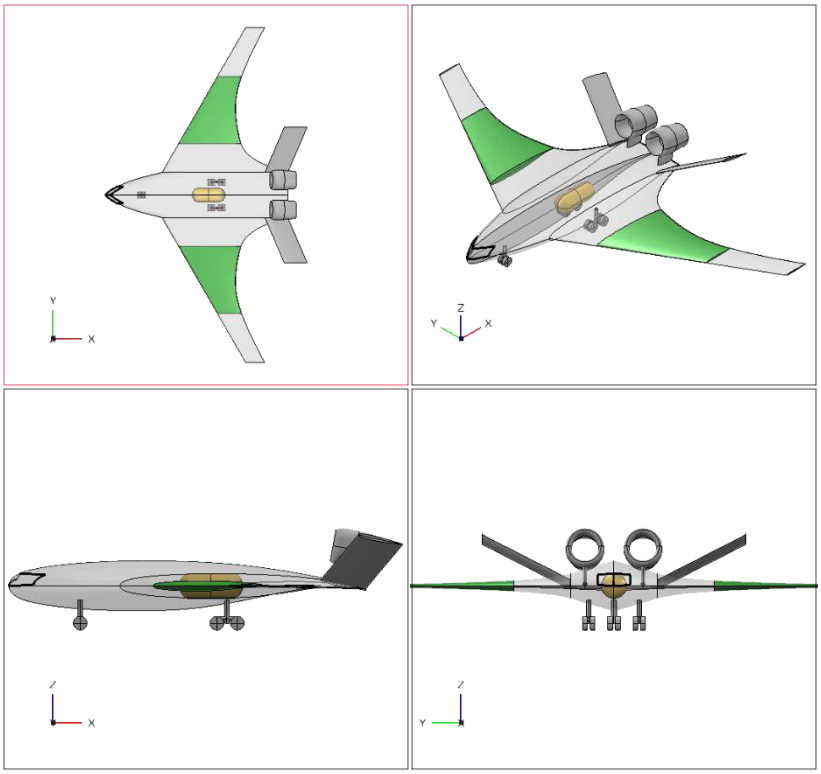

Figure 6-12: Revised Layout Four-View

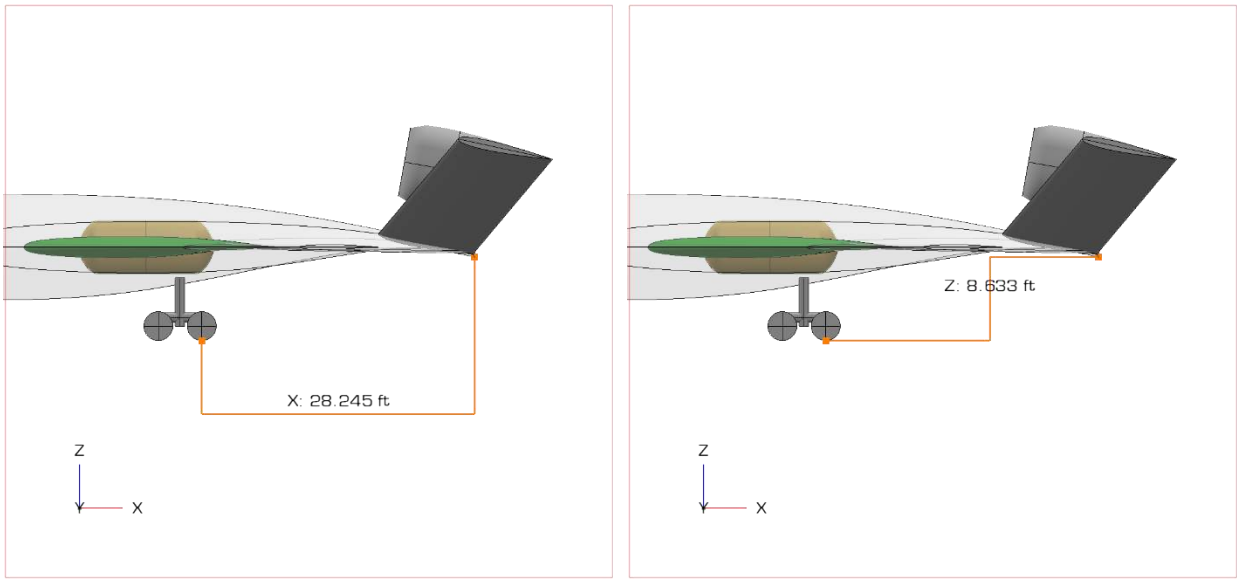

Figure 6-13: Rotation Clearance

Yielding a rotation angle of:

$$\beta_{rot} = \text{atan}\left(\frac{\Delta Z}{\Delta X}\right) \approx 17°$$

Which should be attainable with careful aerodynamic design and high-lift device selection.

Chapter 7 – Aerodynamics

7.1 Introduction

This chapter presents the aerodynamic analysis of the as-drawn aircraft presented in previous chapters. This chapter makes use of analytical methods presented in Raymer, Roskam, and Gudmundsson[9, 11, 23] as well as other classic formulations such as methods from DATCOM[29].

7.2 Clean $C_{L_{max}}$: DATCOM Method

The DATCOM[29] provides an analytical method to calculate the 3D maximum lift-coefficient $C_{L_{max}}$ as a function of Mach number with corrections for sweep and airfoil shape. The method uses the airfoil sharpness parameter, Δy, shown in Figure 7-1:

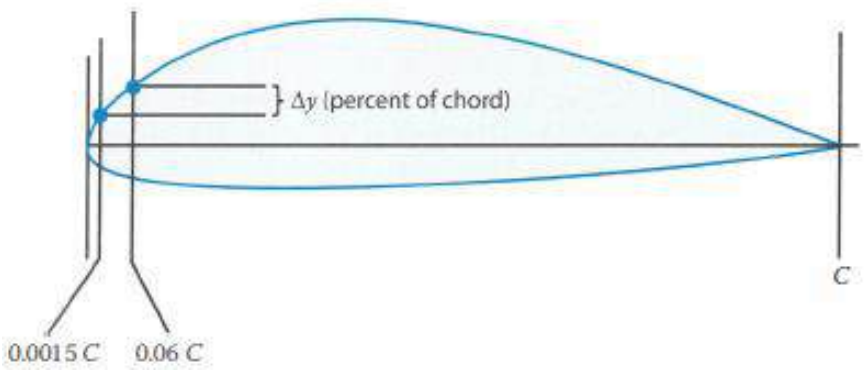

Figure 7-1: Airfoil Sharpness Parameter (Source: Raymer's Aircraft Design: A Conceptual Approach[10])

This is computed for the design airfoil of StratoSOL to be 3.5. The method also classifies aircraft as "high aspect-ratio aircraft" if their aspect ratio satisfies Equation *(29)*:

$$AR > \frac{3}{(C_1 + 1)(\cos \Lambda_{L.E.})} \tag{29}$$

Where C_1 is a constant and is a function of the aircraft's taper ratio. StratoSOL satisfies the condition for high aspect ratio. Therefore, it is possible to use the airfoil sharpness parameter Δy to find corrections of maximum lift-coefficient as a function of Mach number for a given leading edge sweep.

Per DATCOM, the maximum lift coefficient at a given Mach number is computed per Equation *(30)*:

$$C_{L_{max}} = C_{l_{max}} \left(\frac{C_{L_{max}}}{C_{l_{max}}} \right) + \Delta C_{L_{max}} \tag{30}$$

Where the left term is the low-subsonic maximum lift-coefficient and is a function of the sectional maximum lift. The term $\left(\frac{C_{L_{max}}}{C_{l_{max}}} \right)$ is simply the ratio between 3D and 2D maximum lift coefficient and is a function of the sharpness parameter for typical families of airfoils.

The second term, $\Delta C_{L_{max}}$, are the corrections for high-subsonic and transonic speeds. DATCOM only provides values for leading edge sweeps of 20 and 40 degrees, respectively, and does not cover the entire range of Mach numbers desired. Therefore, a logarithmic fit was used to extrapolate values for the corrections. These fits are shown in Equations *(31)* and *(32)*:

$$\Delta C_{L_{max,20^\circ}} = -0.352 \log M - 0.5628 \tag{31}$$

$$\Delta C_{L_{max,40^\circ}} = -0.191 \log M - 0.2948 \tag{32}$$

And are plotted in Figure 7-2 comparing some measured values from the DATCOM correlations and how well the equation fit matches the values:

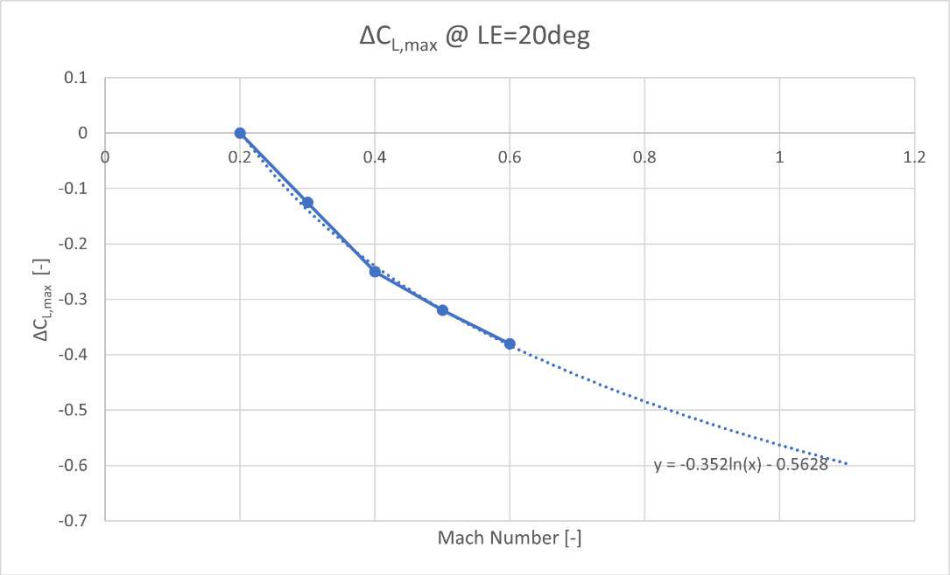

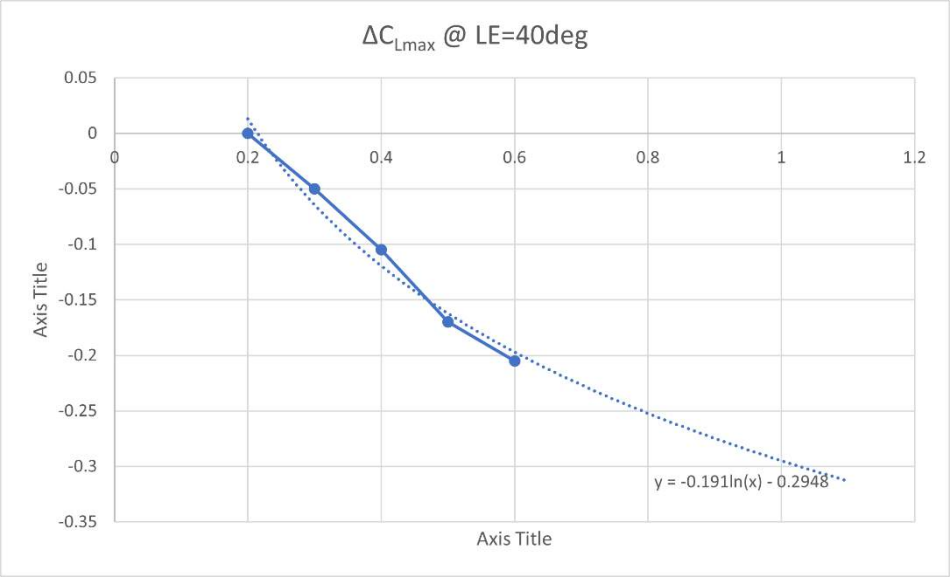

Figure 7-2: Extrapolated $\Delta C_{L_{max}}$ correlations

And, for the sweep of 30 degrees of StratoSOL, the value between the two curves is interpolated, that is:

$$\Delta C_{L_{max,30^\circ}} = \Delta C_{L_{max,20^\circ}} + \left(\frac{40-30}{40-20}\right)(\Delta C_{L_{max,40^\circ}} - \Delta C_{L_{max,30^\circ}})$$

Which allows the clean maximum lift coefficient, $C_{L_{max}}$ to be calculated for a range of Mach numbers at the design wing sweep of 30 degrees. These values are plotted in Figure 7-3:

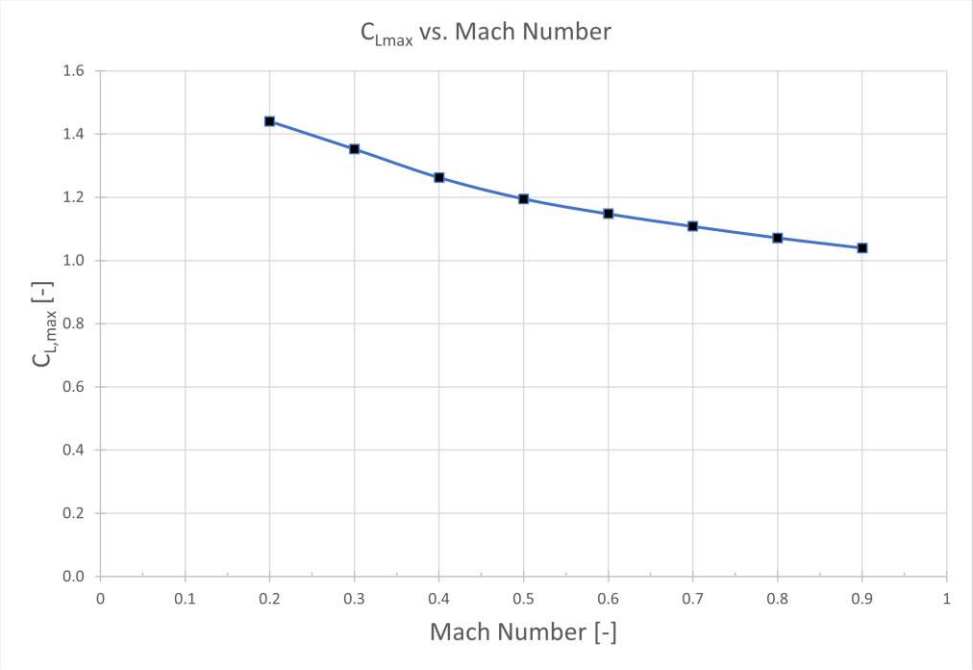

Figure 7-3: $C_{L_{max}}$ versus Mach Number

7.3 High-Lift Devices

DATCOM also provides a simple analytical model for the calculation of the variation in maximum lift coefficient with the use of high-lift devices. It is summarized in Equation *(33)*:

$$\Delta C_{L_{max,flaps}} = 0.9 \Delta C_{l_{max}} \left(\frac{S_{flapped}}{S_{ref}} \right) \cos \Lambda_{H.L} \tag{33}$$

Where $S_{flapped}/S_{ref}$ is the flapped area ratio – the ratio between the area of the planform that is flapped and the total reference area. The term $\cos \Lambda_{H.L}$ is the cosine of the sweep angle formed by the hinge line of the flaps. Finally, the term $\Delta C_{l_{max}}$ is tabulated in Raymer and adapted in Table 7-1:

Table 7-1: Lift Contribution from High-Lift Devices (Source: Aircraft Design: A Conceptual Approach[10])

High-Lift Device	$\Delta C_{l_{max}}$
Plain and Split	0.9
Slotted	1.3
Fowler	1.3 c'/c
Double Slotted	1.6 c'/c
Tripple Slotted	1.9 c'/c

The wetted area ratio is assumed to be around half of StratoSOL's planform. Therefore, a study can be conducted into the effect of different types of high-lift devices on the maximum lift coefficient of StratoSOL for a range of Mach numbers, which takes into account the aircraft's leading edge sweep angle as well as hinge line sweep (both of which contribute negatively to lift.)

Such study is plotted in Figure 7-4:

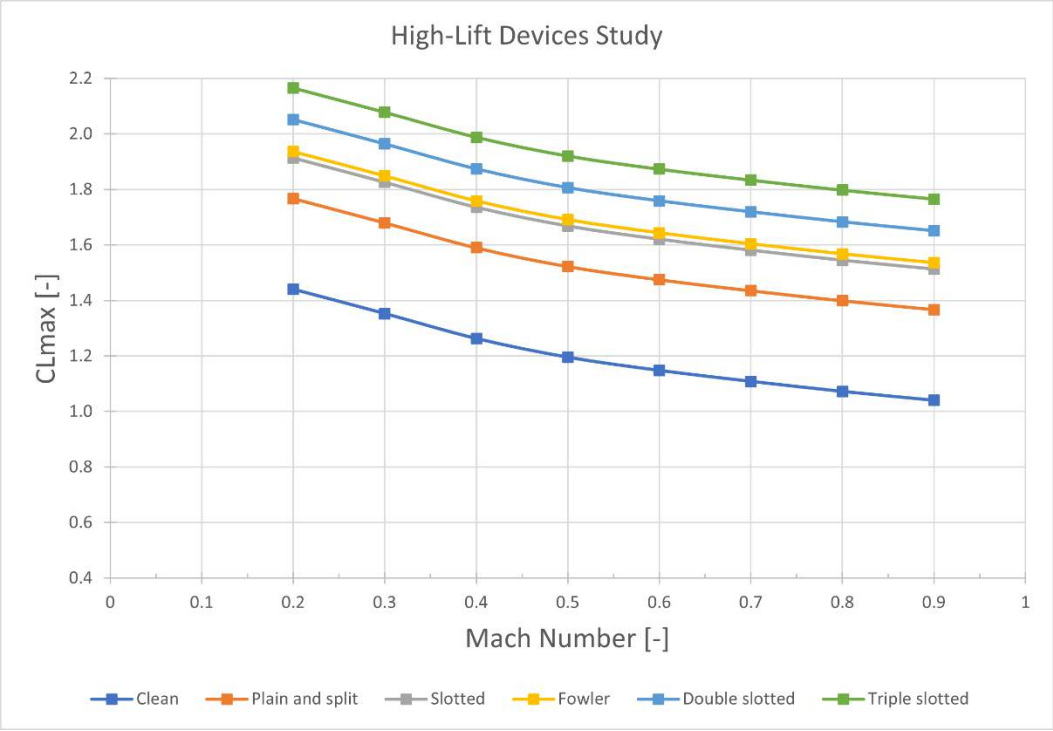

Figure 7-4: High-Lift Devices Study

Constraint analysis showed that takeoff and landing performance are not the most restrictive performance constraints of the design space. Figure 4-3 shows this fact. From those results, it is estimated that a $C_{L_{max}}$ of 1.8 is sufficient to meet the requirements as calculated in the parametric trade studies. Therefore, a single slotted flap geometry spanning half of StratoSOL's planform will suffice.

7.4 Drag Buildup

The parasite drag of StratoSOL can be computed for different configurations using the component drag buildup method, explained at length and in great detail in [9, 11, 23]. The method adds up the parasite drag from each component of the aircraft by calculating its skin friction coefficient C_f and multiplying it by the reference area ratio S_{wet}/S_{ref}. The method also incorporates a form factor correction to account for the viscous effects of drag (pressure drag and separation.)

The drag buildup can be condected in OpenVSP, which calculates the wetted area and applies the skin friction and form factors to the surfaces, yielding it a powerful tool. The drag was computed for three configurations: clean, takeoff, and landing. The clean configuration features no deployed surfaces or landing gears. The takeoff configuration includes the drag from the landing gear and flaps. The landing configuration includes the drag from all takeoff components in addition to spoilers.

For flap drag, Raymer provides Equation *(34)* to calculate the change in parasite drag coefficient:

$$\Delta C_{D_{0,flaps}} = F_{flap}\left(\frac{C_f}{C}\right)\left(\frac{S_{flapped}}{S_{ref}}\right)(\delta_f - 10) \tag{34}$$

Where C_f/C is the flapped chord fraction, and F_{flap} is a constant and equal to 0.0074 for slotted flaps. δ_f is the flap deflection in degrees. Gudmundsson[9] provides a similar method to calculate the drag due to spoilers, shown in Equation *(35)*:

$$\Delta C_{D_{0,spoilers}} = 1.17\frac{b_{sp}h_{sp}}{S}\left(\frac{\delta_{sp}}{90}\right) \tag{35}$$

Where b_{sp} and h_{sp} are the span and height of the spoilers, respectively, and δ_{sp} is the deflection angle of the spoilers in degrees.

Table 7-2 through Table 7-4 show the component-wise drag coefficient, and pie charts of all configurations are shown in Figure 7-5. Figure 7-6 shows the drag polars (coefficients and force) in each configuration.

It is worth to note that the drag polars use a compressibility model developed by Shevell[30]. The model uses a compressible correction factor ΔC_{D_c} such that the total drag coefficient is computed using Equation *(36)*:

$$C_D = C_{D_0} + \left(\frac{1}{\pi e AR}\right) C_L^2 + \Delta C_{D_c} \tag{36}$$

Where the compressibility factor is:

$$\Delta C_{D_c} = [(3.97 \times 10^{-9}) e^{12.7x} + (10^{-40}) e^{81x}] \cos^3 \Lambda \tag{37}$$

Where:

$$x = \frac{M_\infty}{M_{cc,\Lambda=0}} \cos^m \Lambda$$

$$M_{cc,\Lambda=0} = 0.87 - 0.175 C_L - 0.83(t/c)$$

$$m = 0.83 - 0.583 C_L + 0.111 C_L^2$$

This yields a simple yet effective model to account for compressibility effects while taking into account three key aspects of compressible effects: freestream Mach number, leading edge sweep, and airfoil thickness-to-chord ratio.

Table 7-2: Clean Drag Buildup

Clean	
Component	**ΔC_{D_0}**
Wing	0.0052
Tails	0.000753
Engines	0.001037
Interference	0.000699
$C_{D_0} = 0.0077$	

Table 7-3: Takeoff Drag Buildup

Takeoff	
Component	**ΔC_{D_0}**
Wing	0.0052
Tails	0.000753
Engines	0.001037
Landing Gears	0.022837
Flaps	0.015401
Interference	0.004523
$C_{D_0} = 0.0498$	

Table 7-4: Landing Drag Buildup

Landing	
Component	**ΔC_{D_0}**
Wing	0.0052
Tails	0.000753
Engines	0.001037
Landing Gears	0.022837
Flaps	0.015401
Spoilers	0.067447
Interference	0.011267
$C_{D_0} = 0.1239$	

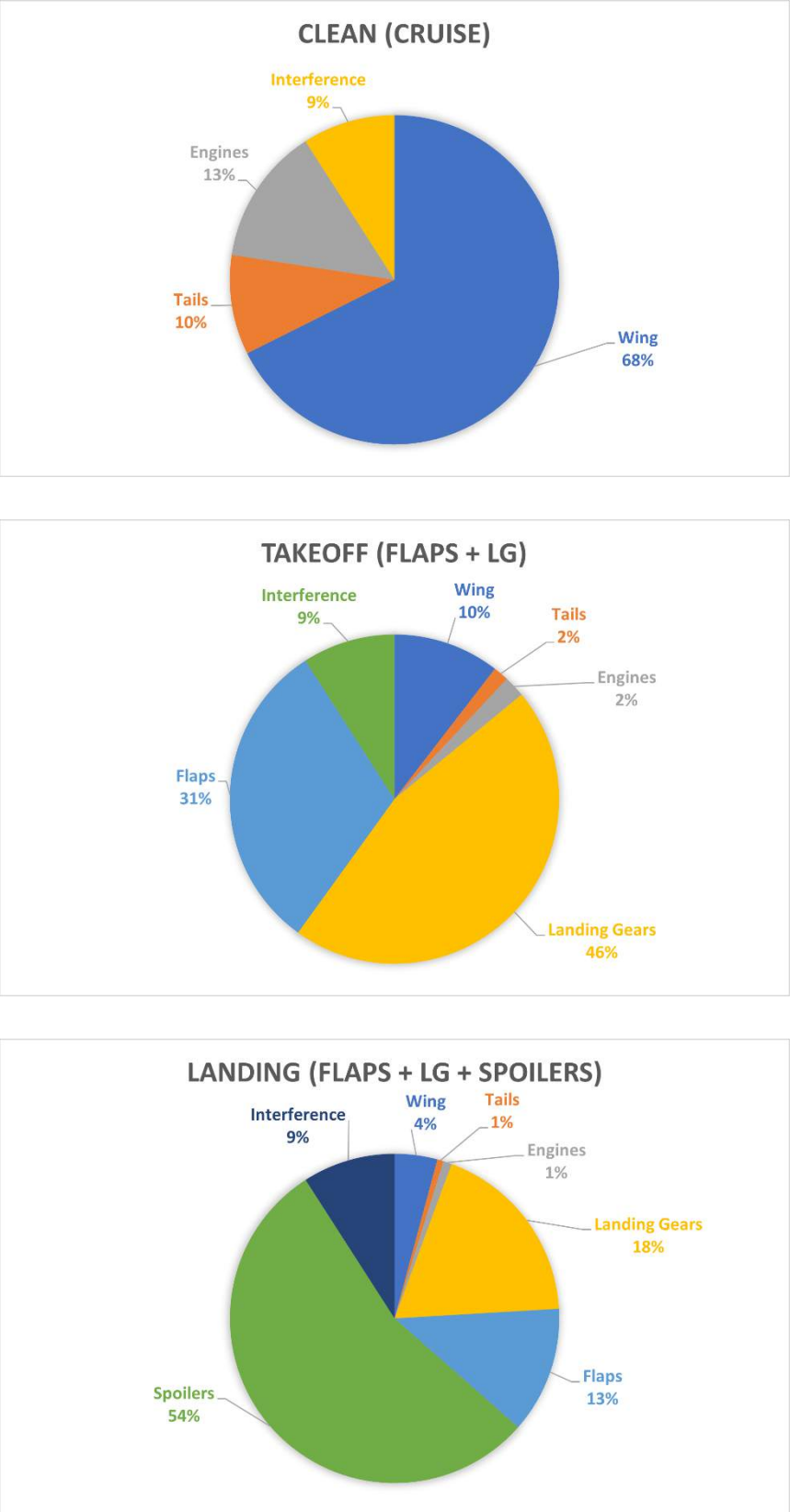

Figure 7-5: Cruise, Takeoff, and Landing Drag Contributions

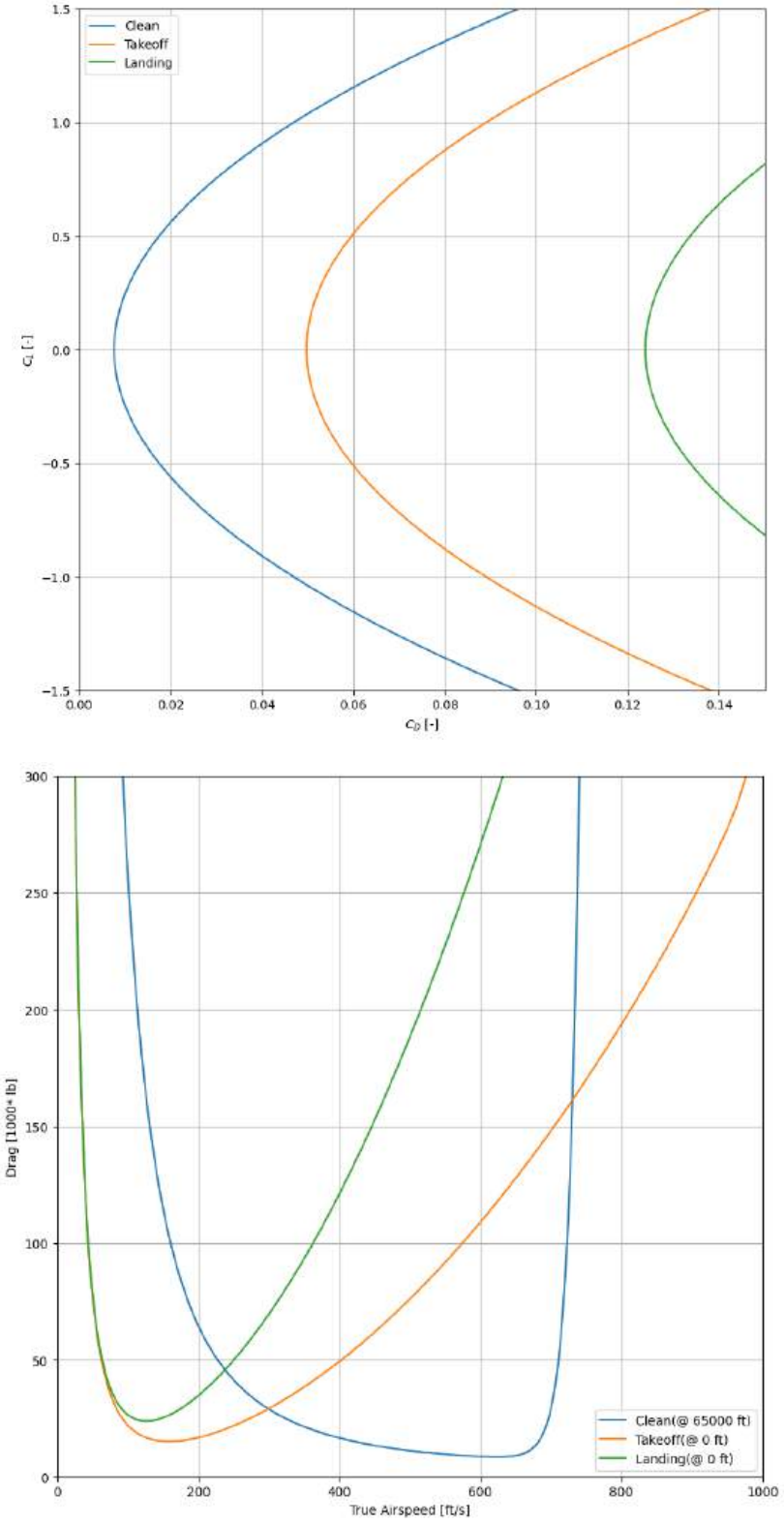

Figure 7-6: StratoSOL Drag Polars

Chapter 8 – Propulsion

8.1 Introduction

Propulsion analysis will aim to investigate altitude and Mach number effects on the available thrust of the selected engine. This author conducted the analysis using two models. First, a scaled representative engine is used to compute thrust losses with methods in Raymer[10]. A more sophisticated model that takes into account the altitude and Mach number variations of both thrust and specific fuel consumption was also used.

8.2 Scaled Representative Engine Method

Engine manufacturers provide the uninstalled thrust curves, which show the thrust output of engines at various Mach numbers and altitudes. However, these curves do not take into account installation-related losses of thrust during practical operation of such engines.

Since engine manufacturer data is not easily obtained for the selected RB211-524H-T, alternative approaches must be taken for propulsion modelling. The appendix of [10] lists several representative engines and their thrust and TSFC curves. This includes a 50,000 lb rated high bypass-ratio (BPR) turbofan. Its curve, digitized by this author, is shown in Figure 8-1:

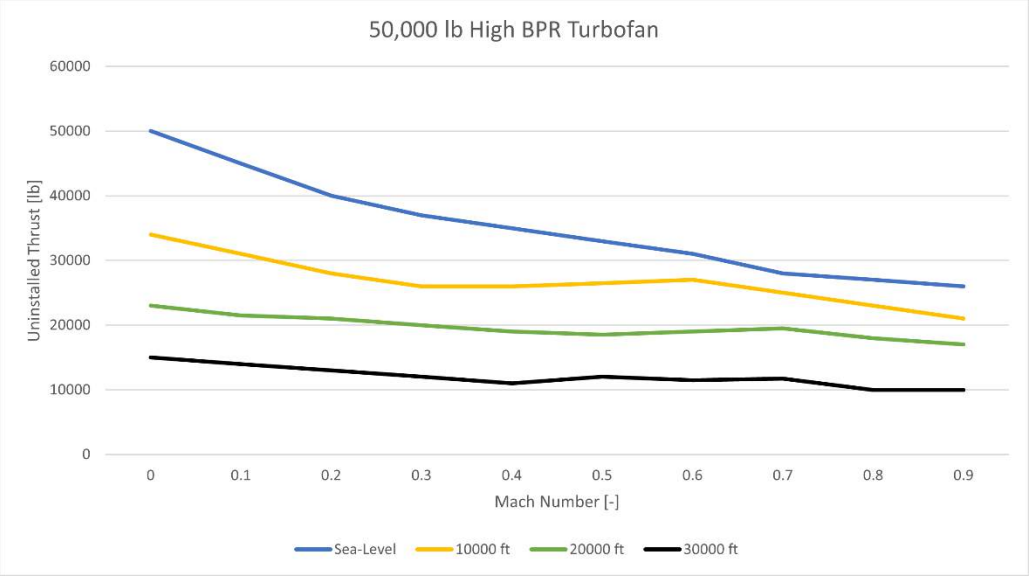

Figure 8-1: Uninstalled Representative High BPR Turbofan

For first-order analysis, the engine's thrust curves can be scaled by the thrust rating of the selected Rolls Royce engine as such:

$$T_{RB211-524} = \left(\frac{T_{RB211-524}}{T_{ref}}\right) T_{ref}$$

And the scaled uninstalled engine thrust curves are shown in Figure 8-2:

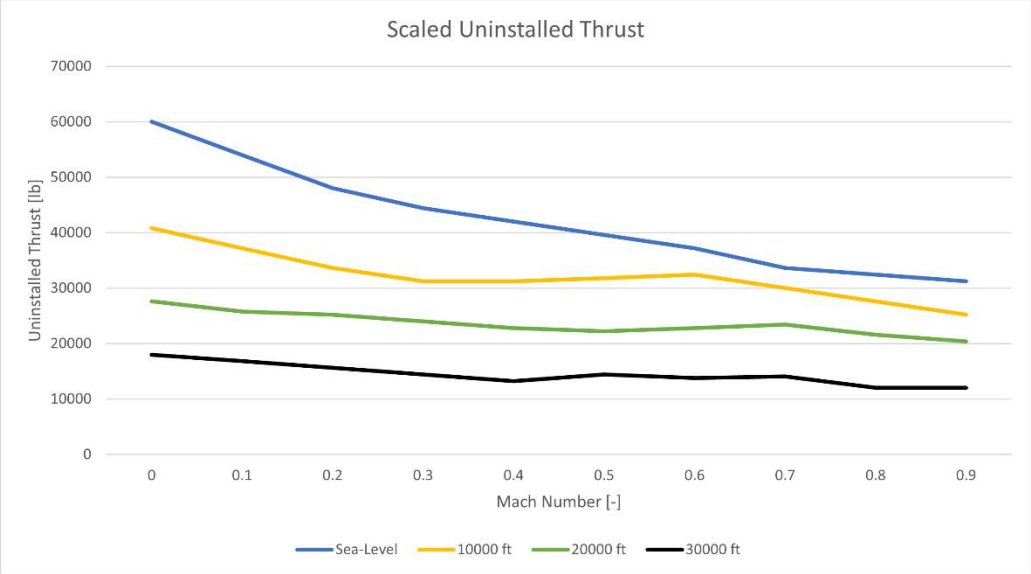

Figure 8-2: Scaled Uninstalled Thrust

Which shows the altitude and Mach number effects of a representative scaled HBR turbofan. Two thrust corrections are provided in Raymer. The first is inlet pressure recovery. The pressure at the inlet's face drops as a consequence of compressible flow dynamics at the sharp edges and curves of the inlet geometry. A thrust loss – or drag – is then created due to the difference in pressure. This can be estimated with Equation *(38)*:

$$\%T_{loss} = C_{ram}\left[\left(\frac{P_1}{P_0}\right)_{ref} - \left(\frac{P_1}{P_0}\right)_{actual}\right] \times 100 \quad (38)$$

However, common inlet designs are able to maintain the pressure loss small enough around the design Mach number of StratoSOL, which is well under supersonic, diminishing these effects. The inlet loss is therefore not considered for this analysis.

The other major thrust loss source is from the bleed air loss in the engine, used for other subsystems of the aircraft. This is usually provided by manufacturer data, but is typically between 1-5%[10]. The loss can be modelled by Equation *(39)*:

$$\%T_{loss} = C_{bleed}\left(\frac{\text{bleed mass flow}}{\text{engine mass flow}}\right) \times 100 \quad (39)$$

The losses were computed and the scaled installed engine thrust curves are plotted in Figure 8-3:

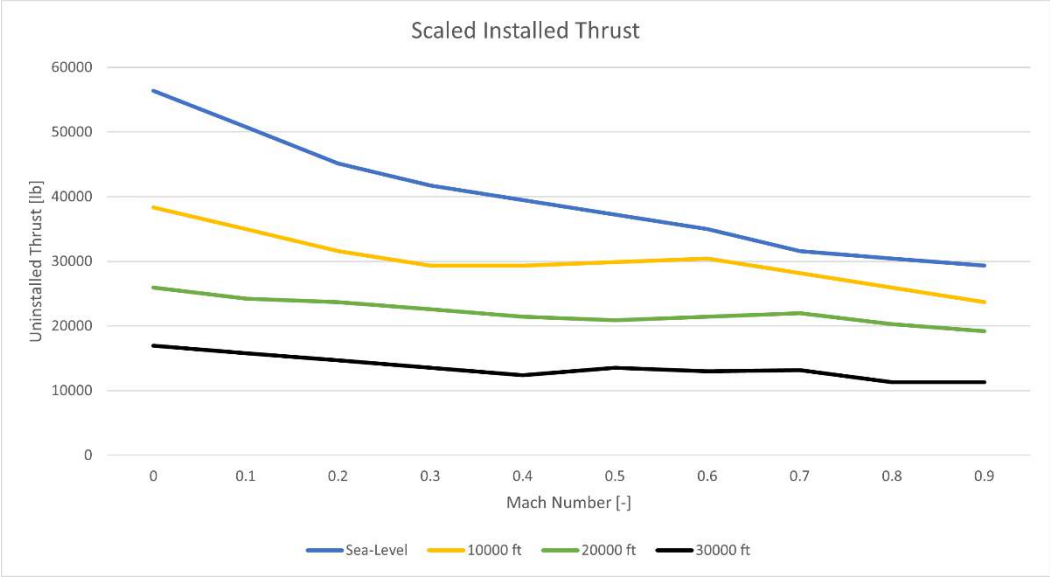

Figure 8-3: Scaled Installed Thrust

8.3 Mattingly's Thrust Model

A more sophisticated model is Mattingly's thrust model for gas turbines[31]. It stipulates the thrust available for a high bypass-ratio turbofan as a function of altitude and Mach dependent parameters. These can be used to calculate the thrust at any given flight condition. The model also includes variations in thrust-specific fuel consumption (TSFC) with Mach number and altitude.

The thrust available with Mattingly's model is shown in Equation *(40)*:

$$T_A = \begin{cases} T_{SL}\delta_0\left[1 - 0.49\sqrt{M_\infty} - \dfrac{3(\theta_0 - TR)}{1.5 + M_\infty}\right] \text{ if } \theta_0 > TR \\ T_{SL}\delta_0\left[1 - 0.49\sqrt{M_\infty}\right] \text{ if } \theta_0 \leq TR \end{cases} \quad (40)$$

Where:

$$\theta_0 = \frac{T}{T_0}\left(1 + \frac{\gamma - 1}{2}M^2\right)$$

$$\delta_0 = \frac{P}{P_0}\left(1 + \frac{\gamma - 1}{2}M^2\right)^{\frac{\gamma}{\gamma - 1}}$$

Are the temperature and pressure ratio, respectively, from isentropic relations, and *TR* is the engine's throttle ratio. The TSFC variation is given by Equation *(41)*:

$$TSFC = (0.45 + 0.54M_\infty)\sqrt{\theta} \quad (41)$$

These can be used to plot the thrust and TSFC curves for the selected engine. The throttle ratio *TR* for high bypass-ratio turbofans usually has as its design point the top-of-climb altitude at cruising airspeeds, and ranges from 0.85 to 1.05[9]. It can also be estimated with Equation *(42)*:

$$TR = \theta\left[1 + \frac{\gamma - 1}{2}M_\infty^2\right] \quad (42)$$

The thrust curves can then be generated. The variation of thrust and TSFC with altitude and Mach number are shown in Figure 8-4:

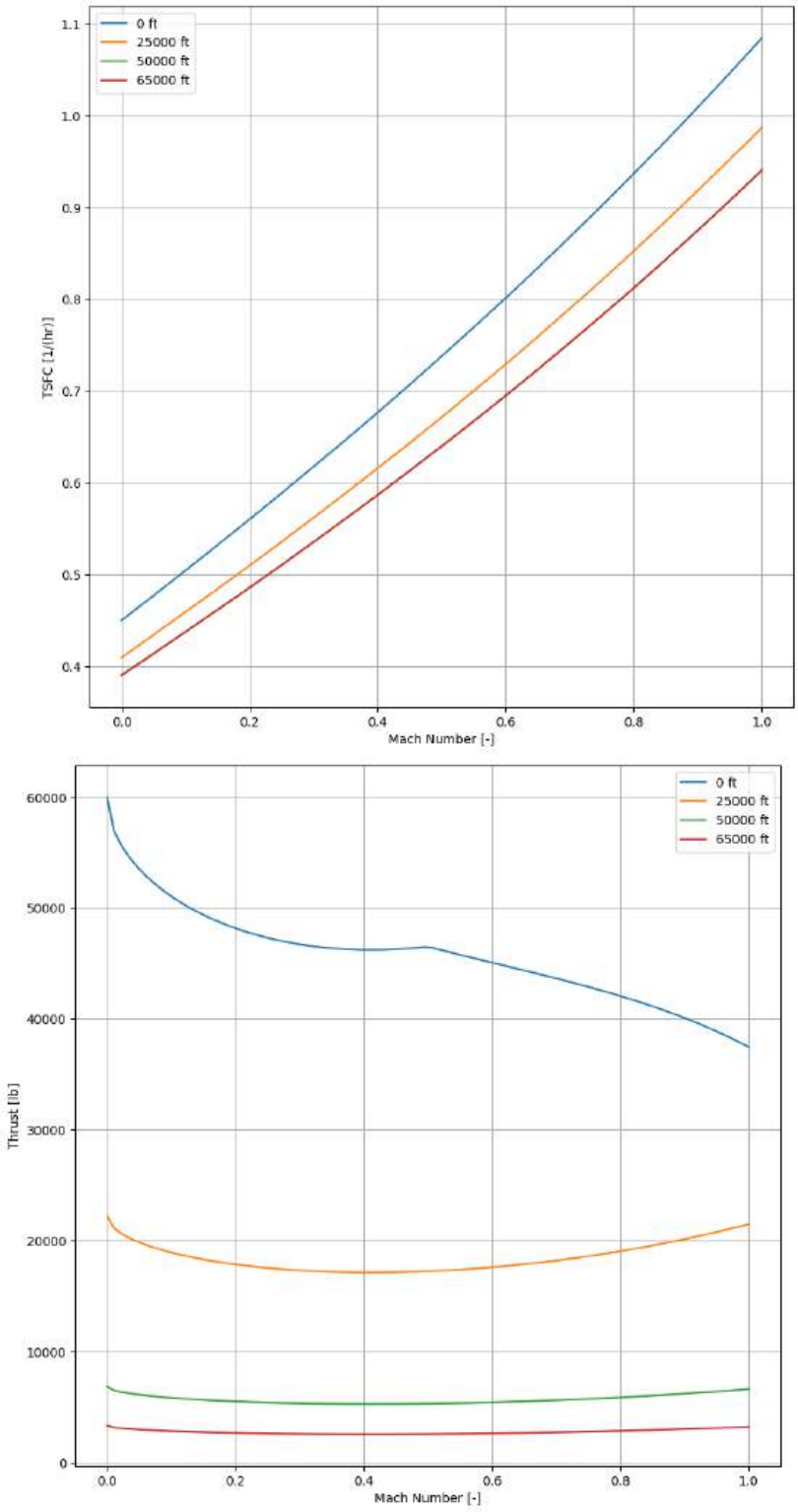

Figure 8-4: Mattingly Thrust and TSFC Curves

Chapter 9 – Structures and Loads

9.1 Introduction

At the conceptual design level, structural analysis consists of material selection and a notional structural layout. At this point, an overview of the expected limits of the flight envelope can also be prepared by means of a V-n diagram. This chapter will show the above.

9.2 Material Selection

The wing and empennage serve the same purpose structurally: to carry the aerodynamic flight loads into the stiffer fuselage structure. In the case of a hybrid-wing body, the "wing" structurally serves the purpose of both the wing and the fuselage. The inner wing (or the "cabin" section of the wing) takes the loads from the more traditional wing structures present towards the tips.

To minimize weight, the use of composites can be considered. Every major aerospace company has now adapted the use of composites for decades. Composites are ideal for the case of StratoSOL's complex compound outer mold line, where any other manufacturing technique would render the geometry or the material unoptimized.

Other materials were also considered. Though composites offer some of the best strength-to-weight ratios currently available, other materials have seen improvements almost comparable to composites. Some aluminum alloys offer great weight savings and can be formed by classic and proven aluminum forming techniques. Such is the case of the Eurofighter Typhoon[10].

For the purpose of StratoSOL, carbon epoxy-fiber was selected for the wing skin as the obvious option for its ability to handle the compound curvatures and excellent strength-to-weight ratio. To reduce the costs of manufacturing, inner wing structures and carry-box structures will utilize instead aluminum-lithium alloys, who offer similar strength-to-weight increases without the expensive cost of composite raw materials and manufacturing.

9.3 Notional Structural Layout

9.3.1 Wing

The wing is composed of three main structural members: the skin, the spars, and the ribs. It is laid out just like a traditional wing structure: the spars carry the main bending loads to the fuselage structure, and the ribs maintain the shape of the composite wing as well as any flexural and buckling loads.

A notional layout of the wing is shown in Figure 9-1. It is composed of two main spars running at the quarter chord and third quarter chords, respectively. Ribs are spaced spanwise.

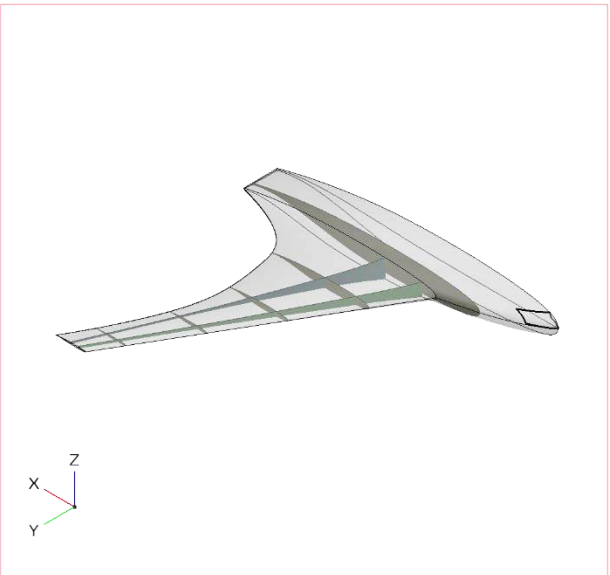

Figure 9-1: Wing Structural Layout

9.3.2 Tails

The structural layout of the tails is similar to that of the wing. The carbon composite skin is supported by an array of aluminum-lithium ribs and spars distributed spanwise along the tails. The structural layout of the tails is shown in Figure 9-2:

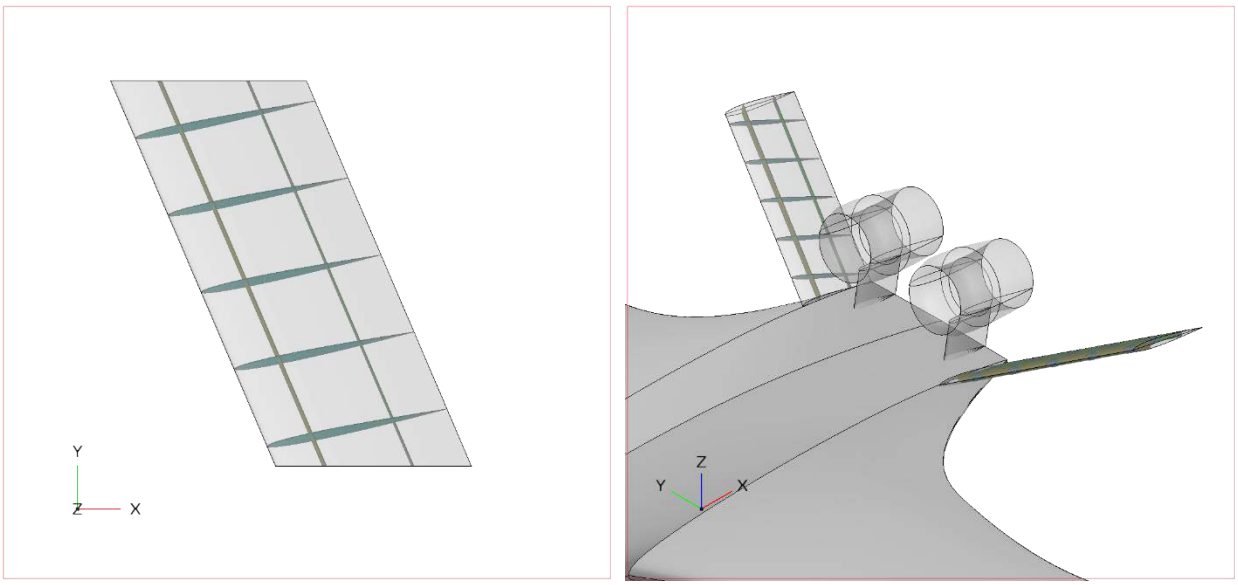

Figure 9-2: Tail Structural Layout

9.3.3 Fuselage/Wing-Body

The wing and tail loads are carried to the fuselage, which contains chord-wise spaced bulkheads and formers, along with spanwise spaced longerons and stringers. The notional layout is shown in Figure 9-3:

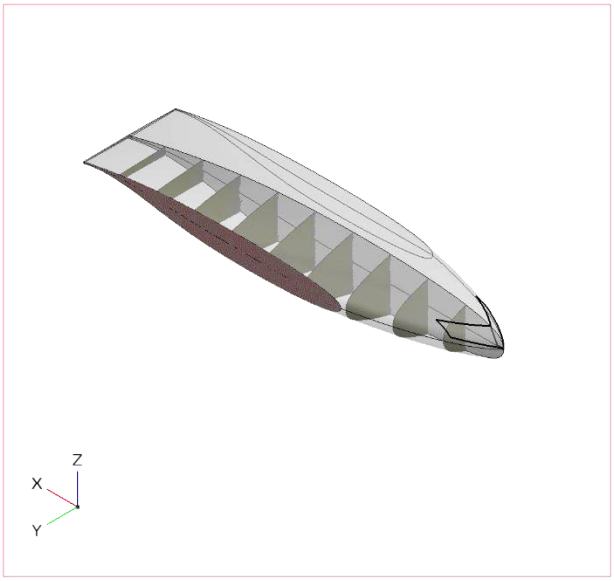

Figure 9-3: Fuselage/Wing-Body Structural Layout

9.4 V-n Diagram

A V-n diagram was prepared for StratoSOL under 14 CFR Part 23 requirements. The diagram shows the aerodynamic (stall) limits of the flight envelope as well as the structural limits. An open-source aircraft design Python-based suite, ADRpy[32], was used. The V-n diagram is shown in Figure 9-4:

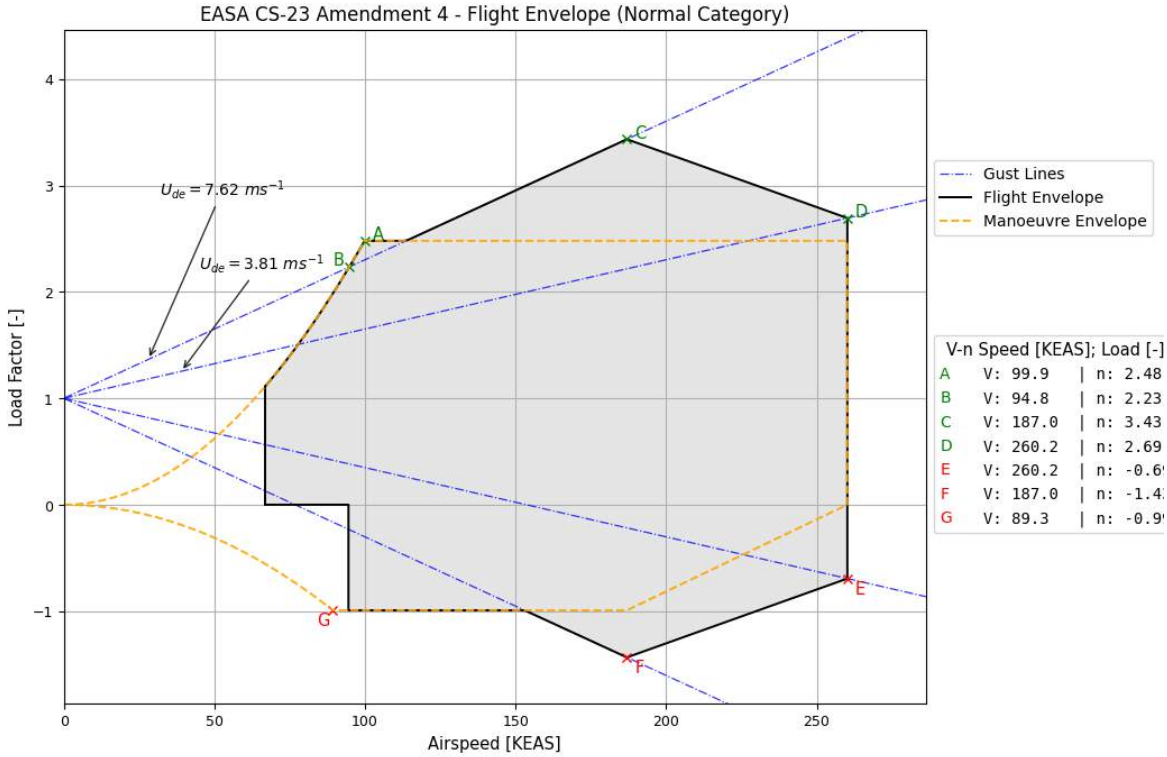

Figure 9-4: StratoSOL V-n Diagram

The figure also highlights both positive and negative V-n limits. Ther are labelled A through G in the diagram above, and are transcribed to Table 9-1 below:

Table 9-1: V-n Diagram Points

Point	V [KEAS]	n
A	99.9	2.48
B	94.8	2.23
C	187.0	3.43
D	260.2	2.69
E	260.2	-0.69
F	187.0	-1.43
G	89.3	-0.99

Where the true gusts experienced are found by taking the product of the derived gust velocities U_{de} shown in the diagram and the gust alleviation factor K_g. The latter is calculated using Equation *(43)*:

$$K_g = \frac{0.88\mu_g}{5.3 + \mu_g} \tag{43}$$

Where μ_g is the mass ratio:

$$\mu_g = \frac{2(WS)}{\rho g \bar{c} C_{L_\alpha}} \tag{44}$$

Chapter 10 – Stability & Control

10.1 Introduction

The goal of stability is to ensure the aircraft can correct any disturbances and return to its original state to maintain its attitude in flight. This chapter deals with the design and analysis for static longitudinal and directional stability. Two main analysis methods are available: analytical methods and computational methods. The basic analytical method for static longitudinal stability comes from the expression shown in Equation *(45)* for the total pitching moment coefficient about the aircraft's center of gravity:

$$C_{M_{cg}} = C_{M_0} + \frac{\partial C_{M_{cg}}}{\partial C_L} C_L + \frac{\partial C_{M_{cg}}}{\partial \delta_e} \delta_e \tag{45}$$

Where the zero AoA pitching moment C_{M_0}, the change in pitching moment with lift coefficient $\partial C_{M_{cg}}/\partial C_L$, and the change in pitching moment with elevator deflection $\partial C_{M_{cg}}/\partial \delta_e$ are given, respectively, by:

$$C_{M_0} = C_{M_{ac}} + a_t(\epsilon_0 + i_w - i_t)\eta_t V_t$$

$$\frac{\partial C_{M_{cg}}}{\partial C_L} = x_{cg} - x_{ac} - \frac{a_t}{a}\eta_t V_t\left(1 - \frac{\partial \epsilon}{\partial C_L}\right)$$

$$\frac{\partial C_{M_{cg}}}{\partial \delta_e} = -a_t \eta_t V_t \tau$$

Each expression is developed in detail, including each term, in Anderson's Introduction to Flight[33].

The other approach, preferred by this author, is to make use of computational methods. These yield results that do not require the assumption of key parameters, such as the variation in downwash with angle of attack, $\partial \epsilon/\partial C_L$, usually obtained in wind tunnel testing. These methods are also easily available, with open-source codes distributed for free online. This chapter will show the stability analysis of StratoSOL using a vortex-lattice computational approach.

10.2 Vortex-Lattice Method

A model of StratoSOL was prepared in AVL[34]. The model takes as an input the geometry and mass properties of the aircraft. The geometry was output from the previously generated XFLR5 model. The mass properties, including moments of inertia, are easily found in OpenVSP, where each object can be assigned a mass, and its distance from the principal axes is known.

Figure 10-1 shows the geometry plot of StratoSOL's AVL model:

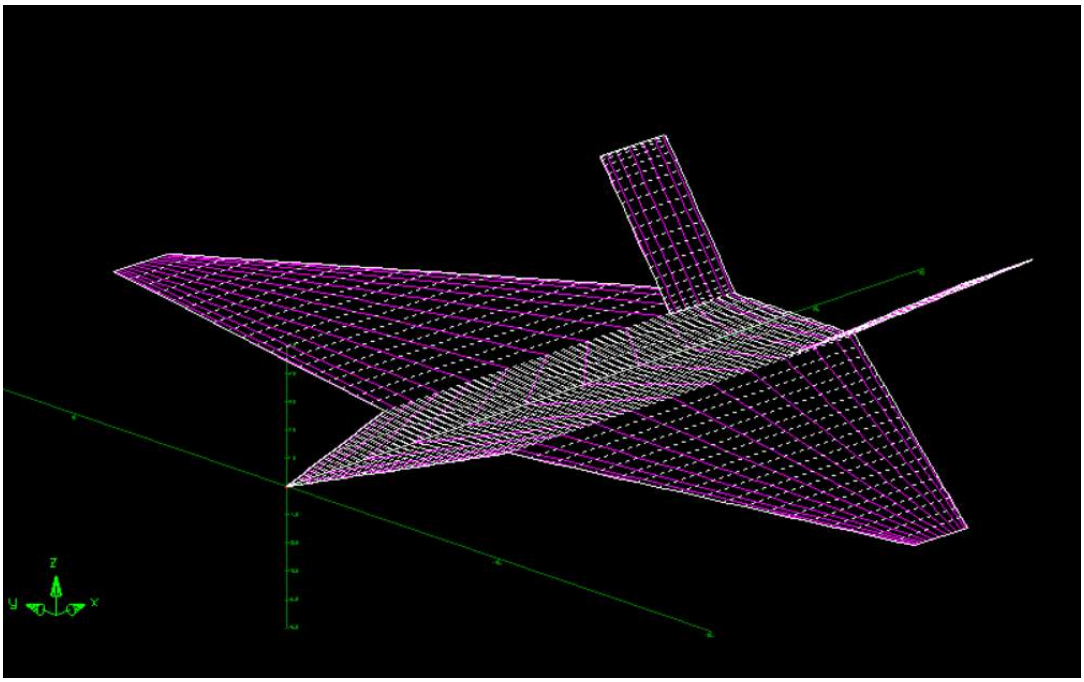

Figure 10-1: StratoSOL AVL Model

The model was run at two conditions: bottom-of-climb and top-of-climb. The assumption is that if the aircraft is able to be trimmed at these high-weight, high-velocity conditions, it is able to maintain level flight throughout the entire mission, with its performance in the corner of the envelope already demonstrated with the V-n diagram.

Figure 10-2 shows the Trefftz-Plane plot of StratoSOL at bottom-of-climb and top-of-climb conditions:

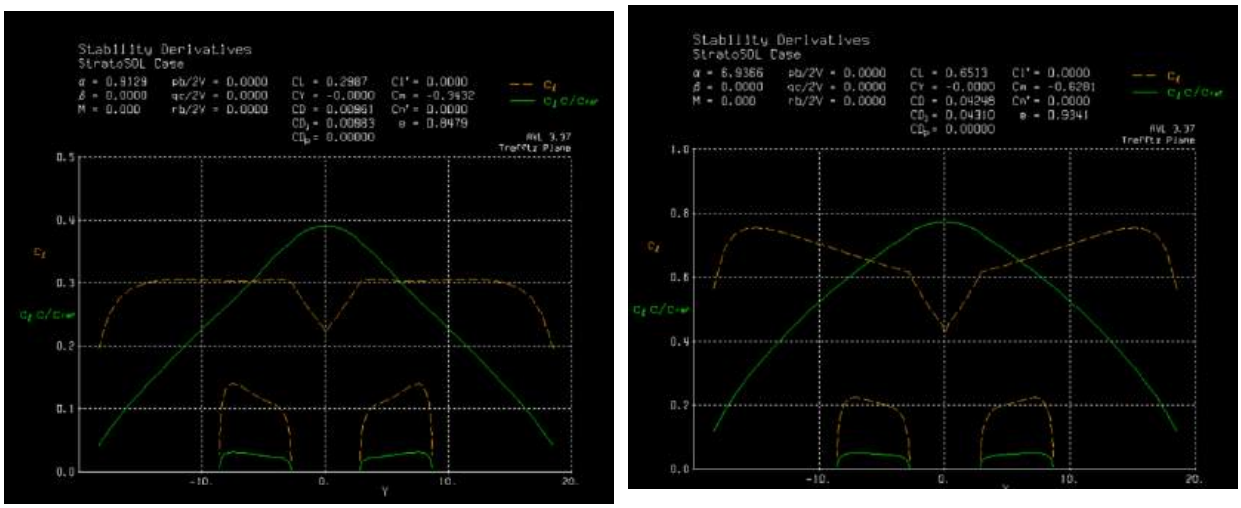

Figure 10-2: Bottom-of-Climb (Left) and Top-of-Climb (Right) Trefftz Plane Plots

And the values are shown in Table 10-1:

Table 10-1: Bottom-of-Climb and Top-of-Climb Trim Conditions

	Parameter	Value
BoC	Oswald Efficiency e	0.8479
	Trim AoA [deg]	0.91
ToC	Oswald Efficiency e	0.9341
	Trim AoA [deg]	6.94

These show that the aircraft is able to achieve trimmed conditions in all flight conditions, assuming no step-climb on a standard day (step climb would be impossible close to service ceiling regardless.)

The aircraft was also analyzed at each static margin designed for in Figure 6-5. It was found to be statically stable in all longitudinal placements. The stability derivatives for one design point, a static margin of 13%, is shown below in Table 10-2:

Table 10-2: Example Stability Derivatives

Stability Derivative	C_{m_α}	C_{l_β}	C_{n_β}
Requirement	**Negative**	**Negative**	**Positive**
Result	-0.53	-0.01	0.29
Meets Requirement?	**YES**	**YES**	**YES**

The table above shows StratoSOL satisfies the requirements for longitudinal and directional static stability. It is worth noting that AVL adopts the "TE down" sign convention, which explains the reason for the reversed signage requirement between the pitching moment coefficient derivative with angle-of-attack C_{m_α} and the yawing moment coefficient derivative with sideslip C_{n_β}.

10.3 Variation of Aerodynamic Center with Mach Number

An important consideration for a pilot at the flight regime of StratoSOL is the notorious "Mach tuck." At transonic and supersonic speeds, the aircraft's aerodynamic center can shift further aft due to the creation of localized shock waves over the wings. This is not an issue for static stability. However, if this change is rapid and significant, it will cause a sudden increase in nose-down moment, which can catch the pilot by surprise.

This variation can be approximated with Equation *(46)*:

$$x_{ac} = x_{c/4} + \Delta x_{ac}\sqrt{S_{wing}} \tag{46}$$

Where the variation in aerodynamic center Δx_{ac} is given by:

$$\Delta x_{ac} = 0.26(M - 0.4)^{2.5}$$

And the variation is plotted in Figure 10-3:

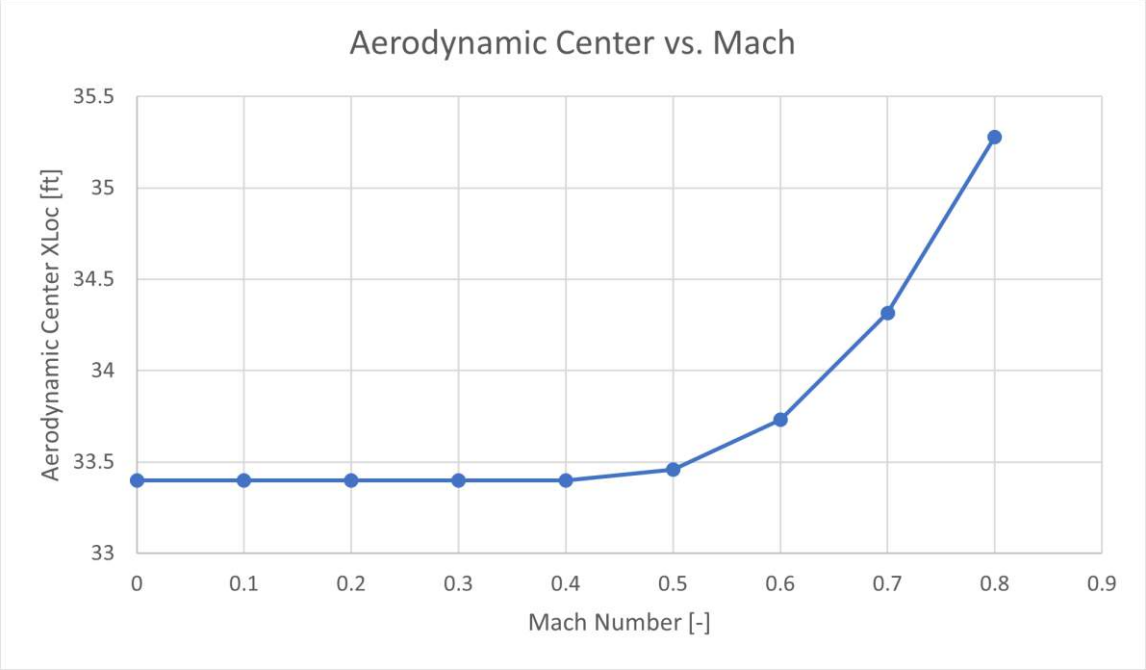

Figure 10-3: Aerodynamic Center versus Mach Number

At the design cruise Mach, the aerodynamic center has moved almost a foot aft as compared to the subsonic longitudinal location. This starts to become significant at airspeeds above the design Mach number, so care must be taken not to abruptly put the aircraft in a nosedive or, even worse, depart the CG envelope and enter uncoordinated flight.

Chapter 11 – Performance Analysis

11.1 Introduction

To verify the performance of StratoSOL, analytical methods found in [9, 10, 21, 33] were incorporated into DSAeroTools to calculate several performance parameters, showing StratoSOL's compliance with requirements.

11.2 Flight Envelope

The flight envelope of StratoSOL can be calculated. For any altitude, the maximum and minimum dynamic pressures can be calculated using the simple analytical expression shown in Equation *(47)*:

$$q_{max,min} = \frac{T_{SL}\sigma(h)}{2C_{D_0}S_{ref}}\left[1 \pm \left(1 - \frac{4kC_{D_0}}{\left(\frac{T_{SL}\sigma(h)}{W}\right)^2}\right)\right]^{1/2} \quad (47)$$

And the flight envelope is shown in Figure 11-1, demonstrating capability of flight at the design condition:

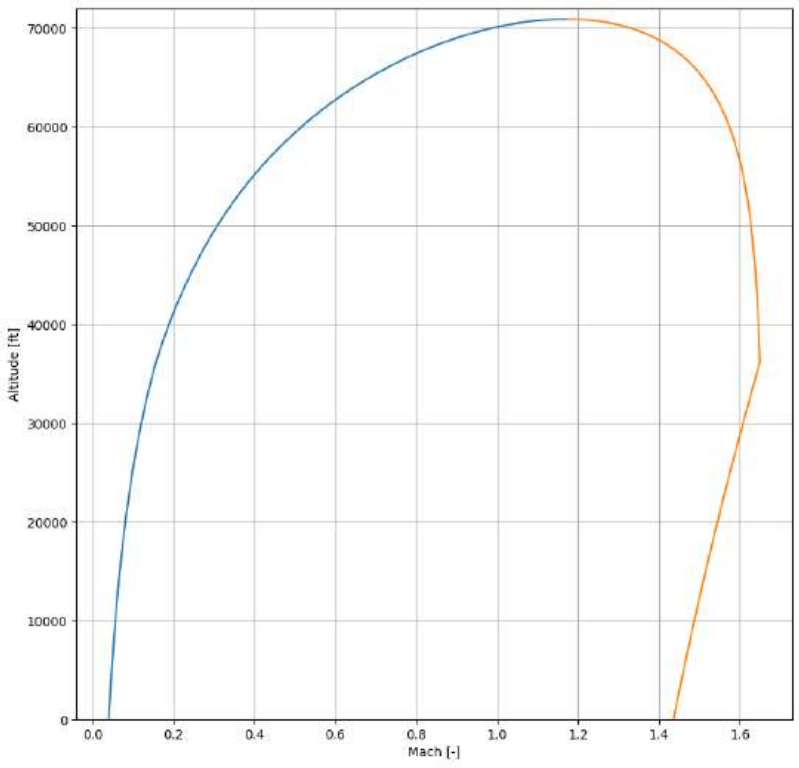

Figure 11-1: StratoSOL Flight Envelope

11.3 Takeoff and Landing Performance

Takeoff and Landing can be modelled analytically using a simplified averaged velocity approach. The takeoff ground run is calculated with Equation *(48)*:

$$S_g = \frac{1.44W^2}{g\rho S_{ref} C_{L_{max}} \{T - [D + \mu_r (W - L)]_{avg}\}} \tag{48}$$

Where the forces shown, that is, thrust, drag, weight, and lift, are averaged over the ground run and can be assumed to be 0.7 times the lift-off speed, which is itself around 1.3 times the stall speed at condition.

The takeoff ground run is computed over a range of altitudes, and is shown in Figure 11-2:

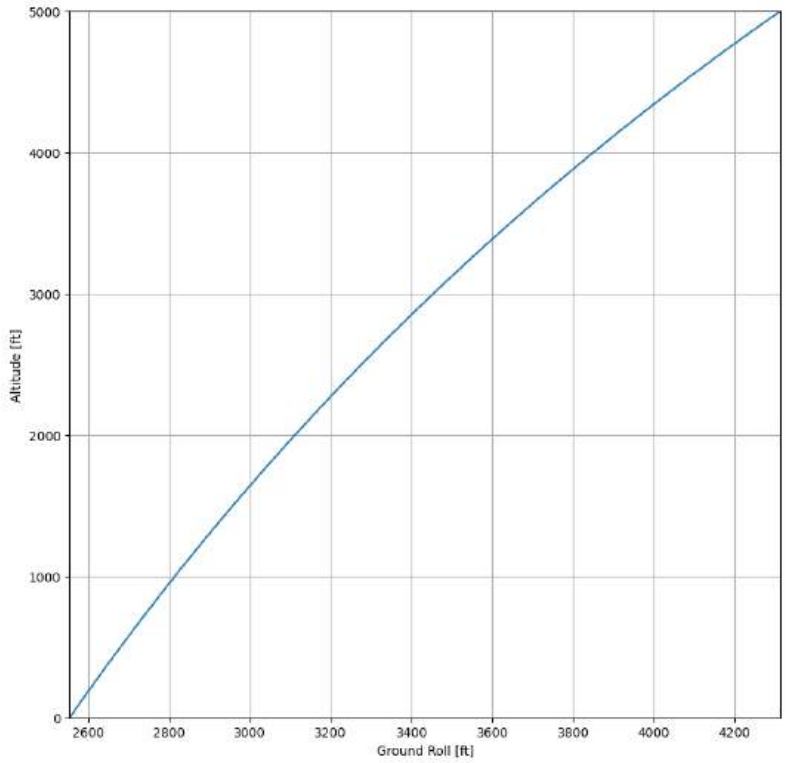

Figure 11-2: StratoSOL Takeoff Ground Roll

Which shows that it meets the required takeoff run with ease, as predicted by constraint analysis. The landing roll was also computed with an equation similar to *(48)*, detailed in Anderson[33]. The landing ground roll with and without the use of thrust reversers is shown in Figure 11-3: StratoSOL Landing Ground Roll:

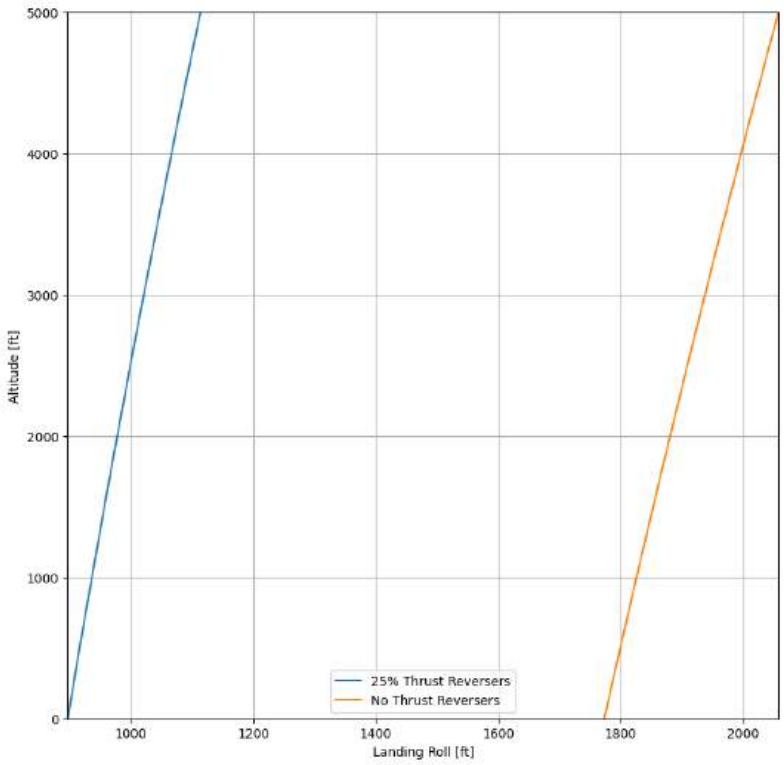

Figure 11-3: StratoSOL Landing Ground Roll

Which also demonstrates that StratoSOL meets landing requirements without the use of thrust reversers. This saves weight due to the reduced complexity of the need of a thrust reversing system, and cuts aircraft certification costs.

11.4 Rate of Climb and Service Ceiling

Lastly, the rate-of-climb over a range of altitudes was computed to verify StratoSOL's capability of climbing to altitude for its 65,000 ft design mission. The rate-of-climb at a given condition and velocity is given by Equation *(49)*:

$$RoC = \frac{V_\infty (T_A - D)}{W} \tag{49}$$

Where T_A is the thrust available, which can be modelled in several ways, some of them detailed in Chapter 8, and D is the drag at condition. These were computed for StratoSOL using the compressible drag model detailed in Chapter 7. The rate-of-climb for a range of altitudes is shown in Figure 11-4:

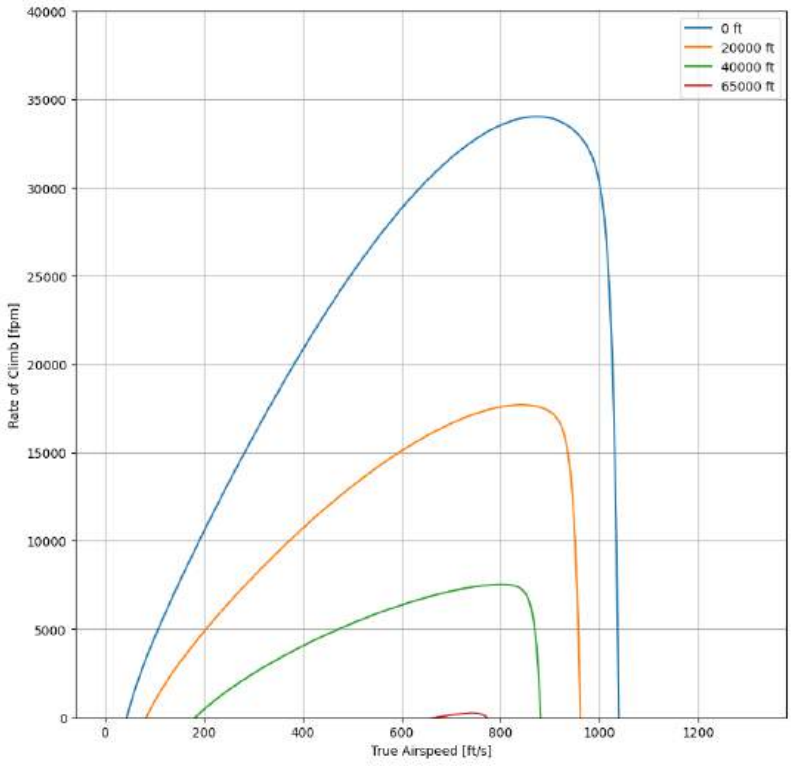

Figure 11-4: StratoSOL Rate of Climb

Which demonstrates it is capable to climb to altitude, and has a service ceiling greater than the design mission requires (65,000 ft). Figure 11-5 shows a close view of RoC at stratospheric altitudes:

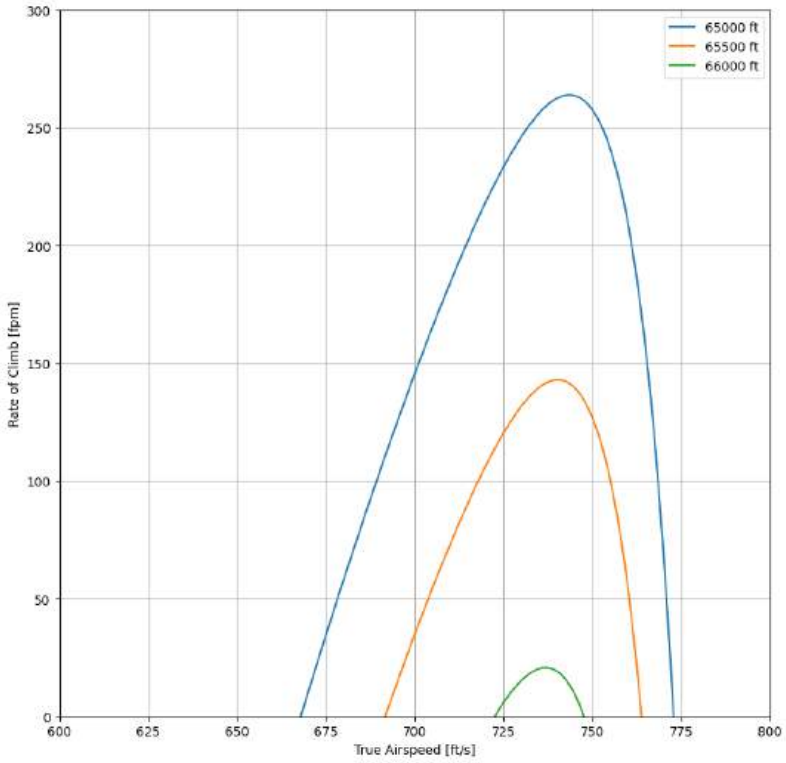

Figure 11-5: StratoSOL Ceiling

Indicating StratoSOL's service ceiling of greater than 65,000ft.

Chapter 12 – Cost Analysis

12.1 RAND DAPCA-IV Model

Cost analysis for StratoSOL was conducted by making use of cost-estimating relationships (CERs.) These are statistical equations obtained from historical aircraft development cost data to predict the costs associated with the development of a new aircraft program. The main advantage of CERs is their simplicity: the most commonly used models require only basic knowledge about an aircraft's weight and velocity to predict a range of required engineering, tooling, and manufacturing hours.

Perhaps the most used set of CERs is RAND's DAPCA-IV model (which stands for "development and procurement costs of aircraft.) It is based on data from the costs of development and production of US Military aircraft. Non surprisingly, it is very biased towards the US market. Furthermore, because it is based on military aircraft, it has a tendency to overestimate the total number of manufacturing hours.

The total cost of an aircraft from conception to disposal is the life-cycle cost. It is the cost from the moment a team of engineers is put together until the last piece of the last aircraft is scrapped. Three important, smaller subsets of the life-cycle cost of an aircraft are of importance to predict in the conceptual design phase: research, development, testing, and evaluation (RDT&E) costs, flyaway costs, and operational costs.

RDT&E costs consist of the engineering hours spent during the research and development of a novel aircraft. This includes prototypes, flight and ground testing, and certification costs. Flyaway costs cover the labor and raw material costs to manufacture the aircraft. This includes the airframe, engines, and avionics. It also includes tooling, and varies significantly with number of units being produced. The more units are produced, the more the "learning curve' comes into effect, decreasing flyaway costs over time. Lastly, operational costs, referred to as operations and maintenance (O&M) cover the costs associated with fuel, oil, crew, maintenance, and insurance, among others.

The analysis below makes use of the RAND DAPCA-IV model. Its expressions are covered in detail in [9, 11] but are omitted here.

12.2 Research, Development, Test & Evaluation (RDT&E) and Flyaway Costs

RDT&E and Flyaway costs were estimated using the DAPCA-IV model. Figure 12-1 shows the expected cost breakdown, with and without novel engine development:

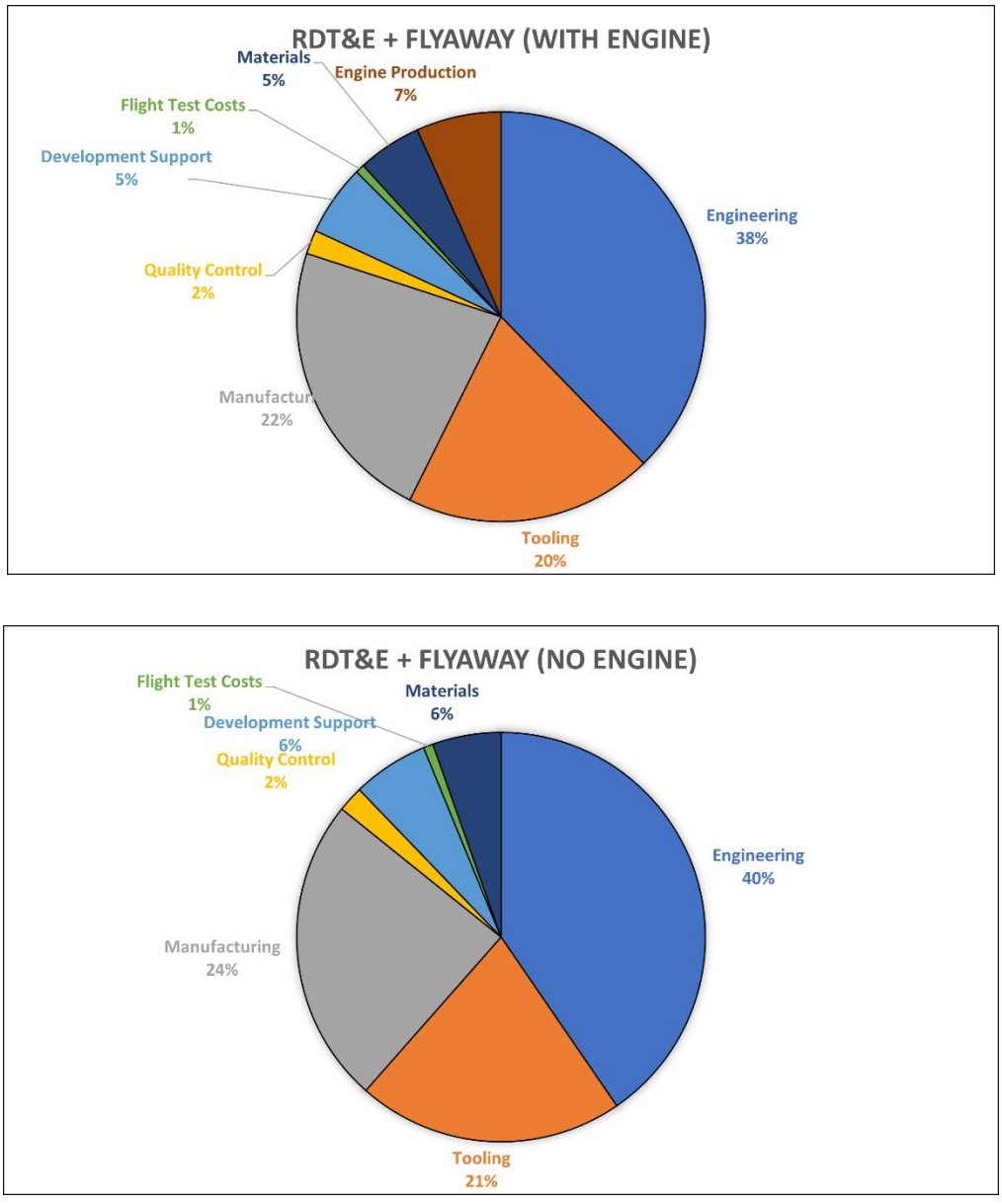

Figure 12-1: RDT&E + Flyaway Costs

And the cost is further broken down in Table 12-1:

Table 12-1: RDT&E + Flyaway Cost Breakdown

Category	Cost
Engineering	$1.3 billion
Tooling	$665 million
Manufacturing	$765 million
Quality Control	$64 million
Development Support	$190 million
Flight Test Costs	$24 million
Materials	$171 million
Engine Production	$227 million
TOTAL (ENGINE)	**$3.4 billion**
TOTAL (NO ENGINE)	**$3.1 billion**

Though the model's accuracy is sometimes suboptimal, these estimates seem to agree with some authors that have explored stratospheric lofters. For these estimates, an initial batch of 10 aircraft including 2 prototype aircraft was assumed. *Smith et al.*[7] arrived at a similar value to that of StratoSOL and based its estimates on private conversations with vendors.

12.3 Operations and Maintenace (O&M) Costs

Two critical O&M costs can be estimated. First, the cost of fuel and oil per aircraft per year can be calculated with Equation *(50)*:

$$C_{f\&o} = (TSFC)(T_0)\left(\frac{FH}{Y}\right)\left(\frac{fuel}{lb}\right) \tag{50}$$

Where $TSFC$ is the thrust-specific fuel consumption, T_0 is the required thrust, and $fuel/lb$ is the cost of fuel per pound, on average. For the values of StratoSOL, and assuming the fleet performs some 4000 flight hours per year as estimated in [7] yields:

$$C_{f\&o} \approx \$8.4 \text{ billion} \frac{1}{(Y)}$$

For the entire fleet of aircraft. The cost of Jet-A on the gallon was found in [35].

Crew costs can also be estimated. Block hours are the operational time of an aircraft from the time the blocks are released from the gears at the origin airport to the time they are put back on the destination airport. Crew costs are notoriously hard to estimate: disruptions and new business models in the world of aviation render these quite variable. Corning[36] provides the following relation using data from Boeing:

$$C_{crew} = 94.5 \left(V_c \frac{W_0}{10^5} \right)^{0.3} + 237.2 \tag{51}$$

Where V_c is the cruise velocity in knots. This is calculated to be:

$$C_{crew} \approx \$574 \frac{1}{\text{block hour}}$$

Chapter 13 – Design Summary and Three-View Diagrams

13.1 Design Summary

Table 13-1 provides a summary of the design of StratoSOL, component by component. Notice that the wing component is the effective wing, as used for the aerodynamic sizing purposes to account for the lift penalty of the fuselage center section:

Table 13-1: StratoSOL Design Summary

	Geometry	Value
Wing	Aspect Ratio (AR)	9.7
	Effective Wing Area (S)	2,108 ft^2
	Wingspan (b)	143.0 ft
	MAC (c)	14.7 ft
	Taper Ratio (λ)	0.4
	LE Sweep Angle ($\Lambda_{L.E.}$)	30 deg
V-Surfaces	Aspect Ratio (AR)	3.3
	Total Surface Area (S)	446.2 ft^2
	Wingspan (b)	44.5 ft
	MAC (c)	10.0 ft
Main Cabin	Max Length	77.4 ft
	Max Width	17.3 ft
	Internal Volume	7200 ft^2
Engines	Manufacturer	Rolls Royce
	Model	RB211-524H-T
	Rated Thrust	60,600 lb
	Weight	9,470 lb

And Table 13-2 provides a summary of StratoSOL's performance metrics, showing its superior performance compared to competition and, most importantly, its compliance with the requirements set forth in the RFP:

Table 13-2: StratoSOL Performance Summary

Performance Metric	Value	Meets Requirement?
Takeoff Ground Roll [ft]	**2554 (SL) 3268 (2500')**	**YES**
Landing Ground Roll [ft]	**1773 (SL) 1908 (2500')**	**YES**
Maximum RoC [fpm]	**> 34,000 (SL) >17,000 (20k)**	**-**
Service Ceiling [ft]	**>65,500**	**YES**
Design Cruise Mach [-]	**0.7**	**YES**
V_Y [ft/s]	**873 (SL) 842 (20k)**	**-**

13.2 Dimensioned Three-View Diagram

Finally, below is a dimensioned three-view diagram showing the dimensions of major aircraft components in its clean configuration:

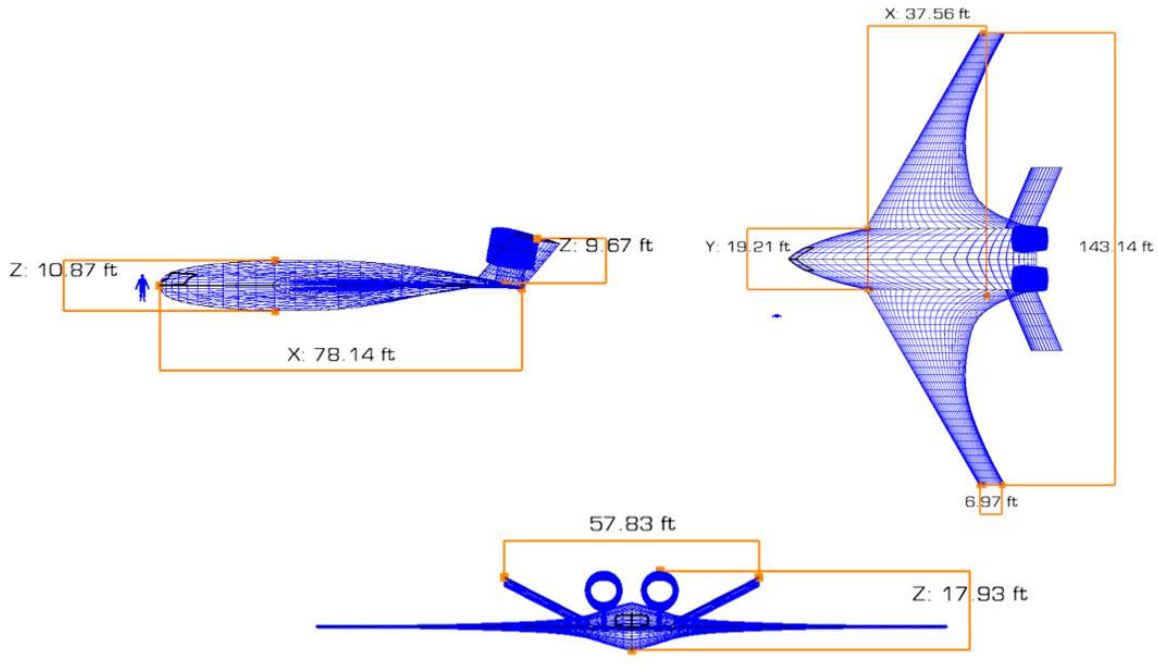

Figure 13-1: Dimensioned Three-View Diagram

Chapter 14 – References

[1]: Trenberth, Kevin E., Fasullo, John T., Kiehl, Jeffrey, “Earth’s Global Energy Balance”, Bulletin of the American Meteorological Society 90, (2009)

[2]: IPCC. (2018). IPCC Special Report: Global Warming of 1.5ºC. https://www.ipcc.ch/sr15/

[3]: Turco, R. P., Toon, O. B., Pollack, J. B., Whitten, R. C., Poppoff, I. G., & Hamill, P. (1980). Stratospheric aerosol modification by Supersonic Transport and space shuttle operations-climate implications. AMETSOC. https://journals.ametsoc.org/view/journals/apme/19/1/1520-0450_1980_019_0078_sambst_2_0_co_2.xml

[4]: Robock, A., MacMartin, D. G., Duren, R., & Christensen, M. (2013). Studying geoengineering with natural and anthropogenic analogs. Climatic Change, 121(3), 445–458. https://doi.org/10.1007/s10584-013-0777-5

[5]: McClellan, Justin, Keith, David W., and Apt, Jay, “Cost Analysis of Stratospheric Albedo Modification Delivery Systems”, Environmental Research Letter 7, (2012)

[6]: AIAA, Undergraduate Individual Aircraft Design RFP – Stratospheric Payload Delivery, https://www.aiaa.org/get-involved/students-educators/Design-Competitions

[7]: Smith, Wake and Wagner, Gernot, “Stratospheric Aerosol Injection Tactics and Costs in the First 15 Years of Deployment”, Environmental Research Letter 13, (2018)

[8]: WB-57 Experimenter's Handbook (PDF). Houston, Texas: NASA Lyndon B. Johnson Space Center. November 2019

[9] Gudmundsson, S., General Aviation Aircraft Design: Applied Methods and Procedures, Butterworth Heinemann, 2013

[10] Raymer, D. P., Aircraft Design: A Conceptual Approach, 6th ed., American Institute of Aeronautics and Astronautics, 2018.

[11] Larrimer, B. Beyond Tube-and-Wing: The X-48 Blended Wing-Body and NASA’s Quest to Reshape Future Transport Aircraft. National Aeronautics and Space Administration.

[12] Airbus. Imagine travelling in this blended wing body aircraft. Airbus. https://www.airbus.com/en/newsroom/stories/2020-11-imagine-travelling-in-this-blended-wing-body-aircraft

[13] JetZero. https://www.jetzero.aero/

[14] Robert A. McDonald and James R. Gloudemans. "Open Vehicle Sketch Pad: An Open Source Parametric Geometry and Analysis Tool for Conceptual Aircraft Design," AIAA 2022-0004. AIAA SCITECH 2022 Forum. January 2022. DOI: 10.2514/6.2022-0004

[15] C.W. Boppe, CFD Drag Prediction for Aerodynamic Design, Technical Status Review on Drag Prediction and Analysis from Computational Fluid Dynamics: State of the Art, AGARD AR 256, June 1989, pp. 8.1–8.27.

[16] Drela, M., XFOIL: An Analysis and Design System for Low Reynolds Number Airfoils, Conference on Low Reynolds Number Airfoil Aerodynamics, University of Notre-Dame, June 1989.

[17] Purser, P., and Campbell, J., "Experimental Verification of a Simplified Vee-Tail Theory and Analysis of Available Data on Complete Models with Vee Tails," NACA 823, 1945.

[18] Bingaman, D. C., Rice, C., Smith, W., & Vogel, P. (2020). A stratospheric aerosol injection Lofter Aircraft Concept: Brimstone Angel. AIAA Scitech 2020 Forum. https://doi.org/10.2514/6.2020-0618

[19] RB211-524G/H & -T. https://www.rolls-royce.com/products-and-services/civil-aerospace/widebody/rb211-524gh-and-t.aspx#section-overview

[20] Gas turbine engines. https://bemil.chosun.com/nbrd/data/10040/upfile/201012/20101222190829.pdf

[21] Roskam, J., Airplane Design Parts I-VIII, DARcorporation, Lawrence, KS, 2018.

[22] xflr5. http://www.xflr5.tech/xflr5.htm

[23] Okonkwo, P. P. C. (2016). Conceptual Design Methodology for Blended Wing Body Aircraft [Ph.D Thesis]. Cranfield University.

[24] KR Bradley. A Sizing Methodology for the Conceptual Design of Blended Wing Body Transports. Technical report, NASA, 2004.

[25] D Howe. The Prediction of Aircraft Wing Mass. Proc. Instn Mech. Engrs, Part G, Journal of Aerospace Engineering, 210(G3):135–145, 1996.

[26] L.R Jenkinson, P Simpkin, and D Rhodes. Civil Aircraft Design. Butterworth Heinemann Publications, 2003.

[27] E Torenbeek. Synthesis of Subsonic Airplane Design. Kluvwer Academic Publishers, Dordrecht, The Netherlands, 1982.

[28] AK Kundu. Aircraft Design. Cambridge University Press, New York, 2010.

[29] Carmichael, R. (2022, October 17). USAF Digital Datcom. https://www.pdas.com/datcom.html

[30] Shevell, R. S., Bayan, F. P., & NASA-Ames Research Center. (1980). Development of a method for predicting the drag divergence Mach number and the drag due to compressibility for conventional and supercritical wings. https://htext.stanford.edu/dd-ill/drag-divergence.pdf

[31] J.D. Mattingly, W.H. Heiser, D.T. Pratt, Aircraft Engine Design, 2nded., AIAA Education Series, 2002.

[32] Sobester, A., ADRpy, https://github.com/sobester/ADRpy

[33] Anderson, John D., Jr. 2016. Introduction to Flight, 8th edition. USA: McGraw-Hill.

[34] Drela, M. and Youngren, H., AVL (3.30) User Primer, AVL Overview, http://web.mit.edu/drela/Public/web/avl/avl_doc.txt

[35] Jet fuel Price Monitor. https://www.iata.org/en/publications/economics/fuel-monitor/

[36] Corning, G., "Supersonic and Subsonic, CTOL and VTOL, Airplane Design," Published by Author, 1976.